Field-induced anomalous magnetic state beyond the magnetically ordered state in the slightly distorted triangular $S = \frac{1}{2}$ rare-earth antiferromagnet CeZn$_3$P$_3$

A. Ochiai, N. Kabeya,[*] K. Maniwa, and M. Saito
Department of Physics, Tohoku University, Sendai 980-8578, Japan

S. Nakamura
Institute for Materials Research, Tohoku University, Sendai 980-8577, Japan

K. Katoh
Department of Applied Physics, National Defense Academy, Yokosuka 239-8686, Japan

(Received 2 August 2021; revised 10 September 2021; accepted 4 October 2021; published 22 October 2021)

Magnetic properties of CeZn$_3$P$_3$, which has been believed to have the same hexagonal ScAl$_3$C$_3$-type crystal structure as that of a spin dimer system of YbAl$_3$C$_3$ at room temperature, have been investigated by magnetization, magnetostriction, specific heat (C), and magnetocaloric effect measurements. In this research, we have found that CeZn$_3$P$_3$ certainly has a slightly deformed crystal structure from the hexagonal one even at room temperature, which is in contrast to the structural phase transition of YbAl$_3$C$_3$ occuring at around 80 K, although the very slight deformation along the c plane, i.e., slightly deformed triangular lattice, and the formation of the multidomain structure are common to both compounds. CeZn$_3$P$_3$ is thought to maintain its deformed structure from a high-temperature region above room temperature to an extremely low-temperature region and shows a magnetic order below $T_{\mathrm{N}} = 0.8$ K. The analysis of the temperature dependence of the magnetic susceptibility (χ) and C has revealed that a Kramers doublet ground state with an easy-plane type anisotropy on the c plane is well isolated from the excited states by the crystal field splitting energy of more than 300 K. Above T_{N}, χ makes a broad peak at around 2 K, which certainly originates from the dimer formation due to the slight deformation of the triangular lattice. On the other hand, below T_{N}, a magnetic phase diagram reminiscent of a magnetic flower blooming on the c plane was observed, which may have a close relation to a quantum effect of a quasi $S = \frac{1}{2}$ spin system and a contribution of the orbital component. With increasing magnetic field, we have found an anomalous magnetic state beyond the usual magnetically ordered state, where C/T is anomalously enhanced. This anomalous magnetic state is similar to that observed in YbAl$_3$C$_3$ induced by the field, although the magnetic ground state in YbAl$_3$C$_3$ is a nonmagnetic dimer state different from the normal magnetically ordered state in CeZn$_3$P$_3$.

DOI: 10.1103/PhysRevB.104.144420

I. INTRODUCTION

In free rare-earth ions, the total angular momentum $\boldsymbol{J}$, which is a combination of the spin angular momentum $\boldsymbol{S}$ and orbital angular momentum $\boldsymbol{L}$ coupled by the spin-orbit interaction, is a good quantum number representing a magnetic state of $4f$ electrons. In real materials, a $2J+1$-fold degenerated state labeled by the total angular momentum $\boldsymbol{J}$ splits up by the crystalline electric field (CEF), which is usually weaker than the spin-orbit interaction for the rare-earth ions. When the number of the $4f$ electrons is odd, at least twofold degeneracy ascribed to the time-reversal symmetry must remain even under extremely asymmetric CEF. The ground state of this twofold degenerated state, i.e., Kramers doublet, is comparable to an $S = \frac{1}{2}$ spin state if the excited states are far enough away from it. In fact, the Kramers doublet is described as an effective spin $S = \frac{1}{2}$ system which is chosen so the degeneracy is set equal to $2S + 1 = 2$ although it includes not only the spin but also the orbital contribution.

It is well-known that the quantum effect is expected to be significant for lower spin states such as the $S = \frac{1}{2}$ spin system; however, the Kramers doublet in the $4f$-electron system has not been almost minded as a quantum spin system until recently, which is in marked contrast to the well-investigated d-electron quantum spin system. Here, we should note that the magnetic state of the Kramers doublet in the $4f$-electron system is usually quite anisotropic, reflecting the spin-orbit entanglement owing to the strong spin-orbit interaction. Therefore, it has been believed that the exchange interaction between the Kramers doublets is expected to be quite anisotropic, reflecting the anisotropic magnetic state due to the spin-orbit entanglement. This is because such a situation can be considered as follows.

Under the strong spin-orbit interaction, as a good quantum number for the $4f$-electron system is not $\boldsymbol{S}$ but $\boldsymbol{J}$, the strength of the exchange interaction is represented by the de Gennes factor $(g_J - 1)^2\boldsymbol{J}\cdot\boldsymbol{J} = (g_J - 1)^2J(J + 1)$, using

---

[*] Corresponding author: kabeya.noriyuki@mail.clts.tohoku.ac.jp

$(g_J - 1)\boldsymbol{J}$ for the conservative part of the spin $\boldsymbol{S}$. This means that the exchange interaction is proportional to square of the magnetic moment, because the magnetic moment is proportional to $\boldsymbol{J}$ ($\because \boldsymbol{\mu} = g_J \mu_B \boldsymbol{J}$). Therefore, thinking naively, if the magnetic moment is anisotropic, it seems good to think that its anisotropy will be reflected in the exchange interaction. That is, the anisotropy of the Kramers doublet will be reflected in the exchange interaction. If higher-order interactions can be ignored, the exchange interactions between the Kramers doublets can be described by the following Hamiltonian using the effective spin $S = \frac{1}{2}$ and using the effective g factors of g_x, g_y, and g_z, of which magnitude reflects the anisotropy of the magnetic moment:

$$H = \sum_{\langle ij \rangle} \left(\mathsf{J}_x g_x^2 s_i^x s_j^x + \mathsf{J}_y g_y^2 s_i^y s_j^y + \mathsf{J}_z g_z^2 s_i^z s_j^z \right). \tag{1}$$

Therefore, even when the exchange coupling constant is isotropic, i.e., $\mathsf{J}_x = \mathsf{J}_y = \mathsf{J}_z$, the exchange interaction seems to become anisotropic owing to the anisotropy of the Kramers doublet, i.e., the local symmetry of the rare earth ion. This situation is in contrast to the ideal $S = 1/2$ spin state and also to the d-electron quantum spin system formed by the almost pure spin state.

Anisotropic exchange interaction, which may reflect the strong coupling between the spin and orbital moments, is reported in $\mathrm{YbMgGaO_4}$ [1,2], which is believed to show the spin liquid behavior at low temperatures. This compound has a trigonal crystal structure (space group Rm), where $\mathrm{Yb^{3+}}$ ions form a triangular lattice. The eightfold degenerated $J = 7/2$ state of the $\mathrm{Yb^{3+}}$ ion is split into four Kramers doublets by CEF with D_{3d} local symmetry of the $\mathrm{Yb^{3+}}$ site. Considering the global symmetry around the z axis only, the magnetic properties of this compound are thought to be mainly dominated by the following XXZ model Hamiltonian for the Kramers doublet ground state as an effective spin $S = \frac{1}{2}$ system:

$$H = \mathsf{J} \sum_{\langle ij \rangle} \left(s_i^x s_j^x + s_i^y s_j^y + \Delta s_i^z s_j^z \right). \tag{2}$$

In this compound, the effective g factors parallel and perpendicular to the z axis are estimated as $g_\parallel = 3.06$ and $g_\perp = 3.72$ from the saturated magnetic moments, respectively, and these results lead to anisotropic ratio of $(g_\parallel/g_\perp)^2 = 0.68$, which is much larger than the ratio of the exchange coupling constant $\Delta = \mathsf{J}_x/\mathsf{J}_z = 0.54$ determined from the paramagnetic Curie temperature. This means the exchange anisotropy is larger than the anisotropy of the magnetic moment. In any case, the exchange interaction Hamiltonian is presumed to be quite anisotropic. Recently, another anisotropic $4f$-electron quantum spin system candidate of $\mathrm{NaYbS_2}$ has also been found [3].

Despite the above considerations and actual examples, several $4f$-electron quantum spin systems with isotropic exchange interactions are actually reported although their magnetic moments are quite anisotropic. One such example is $\mathrm{Yb_4As_3}$, which is known as a rare one-dimensional $4f$-electron Heisenberg antiferromagnet reported around the end of the former century [4]. It forms a magnetic $\mathrm{Yb^{3+}}$ chain under the charge-ordered state below room temperature because the chains are well magnetically isolated from each other by nonmagnetic $\mathrm{Yb^{2+}}$ ions [5]. The $J = 7/2$ multiplet of the $\mathrm{Yb^{3+}}$ ion is split into four Kramers doublets by CEF with C_3 local symmetry, of which the threefold axis is parallel to the chain direction. As the first excited doublet lies about 140 K above the ground state, magnetic properties of the $\mathrm{Yb^{3+}}$ ion are dominated by the ground-state Kramers doublet at low temperatures. Considering the threefold symmetry around the chain direction, the spin-1/2 XXZ-type Hamiltonian is expected. In fact, from the neutron-scattering experiment, effective g factors parallel and perpendicular to the chain are estimated to be $g_\parallel = 2.9$ and $g_\perp = 1.3$, respectively [6]. Nevertheless, actually observed spin dispersion spectra in $\mathrm{Yb_4As_3}$ obeys that of the $S = \frac{1}{2}$ one-dimensional Heisenberg antiferromagnet [4,7,8]. The anisotropy of the Kramers doublet may be thought to appear only in the effective g factor when the magnetic field is applied.

A further example of the $S = \frac{1}{2}$ one-dimensional Heisenberg antiferromagnet is $\mathrm{Yb_2Pt_2Pb}$, which shows the antiferromagnetic order around 2 K. The physical properties of this compound suggest a strong Ising-type magnetic moment made mainly by $|J, J_z\rangle = |7/2, \pm 7/2\rangle$; however, the anisotropy of the exchange interaction is thought to be much smaller than that expected from the magnetic field response [9,10]. Actually, Δ of Eq. (2) estimated from the neutron experiment is about 3; however, $(g_\parallel/g_\perp)^2$ is estimated to be about 100 from the effective g factor ($g_\parallel = 7.9$ and $g_\perp = 0.6 \sim 0.8$) determined from the CEF calculation for the Kramers doublet ground state. Here, $g_\parallel$ and $g_\perp$ are effective g factors parallel and perpendicular to the Ising axis of each site. Furthermore, the characteristic spin dispersion similar to that of $\mathrm{Yb_4As_3}$ has been observed by the elastic neutron scattering.

Another example with isotropic exchange interaction may be $\mathrm{YbAl_3C_3}$, which also joins a family of the quantum spin systems in the $4f$-electron compounds; however, it is in a rather complicated situation and takes on a different aspect. $\mathrm{YbAl_3C_3}$ has a hexagonal $\mathrm{ScAl_3C_3}$-type structure (space group $P6_3/mmc$) shown in Fig. 1(a) at room temperature, where $\mathrm{Yb^{3+}}$ ions form a triangular lattice. The local symmetry of the $\mathrm{Yb^{3+}}$ site is D_{3d}. The effective g factors are estimated to be $g_\parallel = 2.26$ and $g_\perp = 2.86$, which indicate an anisotropic ratio of $(g_\parallel/g_\perp)^2 = 0.62$. This compound shows a quite slight crystal deformation from a hexagonal to orthorhombic one by small displacement of the constituent atoms at about 80 K [9,11]. In the low-temperature orthorhombic phase, physical properties such as specific heat (C) and magnetization (M) of $\mathrm{YbAl_3C_3}$ indicate no long-range magnetic order and are well explained by a magnetic energy gap of 15 K. It means that the anisotropic Kramers doublets of $\mathrm{YbAl_3C_3}$ form a magnetic dimer ground state similar to those observed in the d-electron dimer system, which causes a singlet-triplet splitting possibly reflecting isotropic exchange interaction [12,13].

Therefore, in these compounds, it seems that the interaction between the Kramers doublets may be generally isotropic, i.e., a Heisenberg-type exchange interaction. However, the application of magnetic fields can change this situation because it generally breaks the rotational symmetry and changes the wave function of the Kramers doublets. Thus, field-induced states appear to be quite different from those expected from the Heisenberg Hamiltonian. In fact, the anisotropic

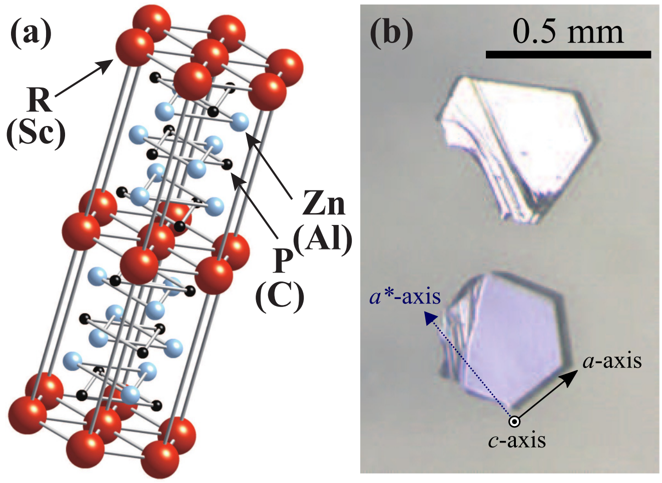

FIG. 1. (a) $ScAl_3C_3$type structure. (b) Photograph of $CeZn_3P_3$ crystal obtained by the flux method. The length of the top solid line corresponds to 0.5 millimeters. Axes representation in the photograph is assigned for the bottom crystal in the $ScAl_3C_3$-type structure.

magnetic field-induced gap is observed in Yb_4As_3 because of no inversion symmetry on the line connecting the Yb^{3+} ions [14]. Phenomena that are decisively different from those of the d-electron system have been found in $YbAl_3C_3$ under the magnetic field. Although magnetic dimers are formed in $YbAl_3C_3$, its field-induced magnetic state is intrinsically different from the field-induced ordered phase (FIOP) of the d-electron dimer system in many respects [15]. For instance, a highly disordered state, where C obeys $-T \ln T$ behavior similar to that of non-Fermi liquid observed in strongly correlated f-electron systems, is induced by the magnetic field. Therefore, C/T appears to be enhanced in such a region. Furthermore, such an anomalous region of $YbAl_3C_3$ is not closed on the magnetic field-temperature (H-T) phase diagram in contrast to the closed FIOP of the d-electron dimer system [16–18]. Such differences may probably be ascribed to the orbital component of the Kramers doublet because it is a characteristic of the twofold degenerated state of the f-electron system in contrast to the d-electron system, but its detail is still an open question [15].

Therefore, to explore a quantum spin system in rare-earth compounds, it is important to examine the anisotropy of the magnetic moment, i.e., the contribution of the orbital moment and how it affects magnetism. Furthermore, it may be also important to examine what the role of the orbital components in the magnetic interaction between the Kramers doublets is. Such orbital components may experimentally realize a quantum state different from those observed in the d-electron system.

RZn_3P_3 ($R =$ Y, La-Nd, Sm, Gd-Er) have been reported to have the same hexagonal $ScAl_3C_3$-type crystal structure (space group $P6_3/mmc$) as that of $YbAl_3C_3$, in which the R ions form triangular sublattices on the $z = 0$ and $z = 1/2$ layers as shown in Fig. 1(a) [19]. The local symmetry of the rare-earth ion site is D_{3d}. In the case of $CeZn_3P_3$, as the Ce ions layer is isolated by the layer composed of Zn and P ions from the next Ce ions layer by a distance of about 10 Å, which is much larger than the length of the triangular side of about 4 Å, the Ce ions layer is expected to be close to an ideal two-dimensional triangular magnet. Although most of the physical properties had not been reported, recently, a preliminary report on RZn_3P_3 was made by our group [20].

In this paper, basic physical properties of $CeZn_3P_3$ under zero or weak magnetic fields will first be introduced. We present magnetic properties of $CeZn_3P_3$ which can be well explained by the doublet ground state with an easy-plane-type magnetic anisotropy. Then we will report sample-dependent specific heat under magnetic fields possibly ascribed to the very slight crystal deformation, which was found in the process of exploring new quantum phases in $CeZn_3P_3$. Finally, we will present a field-induced anomalous magnetic state which locates beyond the magnetically ordered state and discuss the magnetic order of $CeZn_3P_3$ in comparison with the nonmagnetic dimer state in $YbAl_3C_3$.

II. CRYSTAL GROWTH AND EXPERIMENTS

Single crystals of $CeZn_3P_3$ were grown by the flux method using a salt flux (NaCl/KCl=1:1) as described in Ref. [20]. We also prepared $LaZn_3P_3$, the nonmagnetic reference material of $CeZn_3P_3$, by the same method. Single crystals of $CeZn_3P_3$ and $LaZn_3P_3$ obtained take the form of a hexagonal plate reflecting its hexagonal crystal structure with diameters up to several millimeters and a thickness of dozens of micrometers as shown in Fig. 1(b). As the typical weight of the obtained single crystal was less than 1 mg, samples of several pieces together with a total weight of several mg was used in some measurements. Confirmation of the crystal structure of the hexagonal $ScAl_3C_3$-type structure and the lattice constant are as described in Ref. [20], which are in good agreement with values reported previously [19].

Experiments were conducted as follows. The measurement of M in the range of $T \approx 1.8$ K to room temperature was carried out using a superconducting quantum interference device magnetometer. M at low temperatures down to $T \approx 0.5$ K was measured up to $\mu_0 H = 8$ T by the Faraday balance technique using a superconducting magnet with field gradient. For the specific-heat measurement under the magnetic field, the relaxation method and the quasiadiabatic method were used in the ^{4}He cryostat down to $T \approx 1.9$ K and the ^{3}He cryostat down to $T \approx 0.5$ K. On the other hand, for the extremely low-temperature measurement of specific heat, magnetocaloric effect (MCE) and magnetostriction using a strain gauge, a dilution refrigerator was used.

III. RESULT AND DISCUSSION

A. Basic properties of $CeZn_3P_3$

In this subsection, we will introduce basic physical properties of $CeZn_3P_3$ and its reference compound $LaZn_3P_3$ under zero or weak magnetic fields.

The electrical resistivity of $LaZn_3P_3$ and $CeZn_3P_3$ indicates the semiconductive character as reported in our previous report [20], which suggests that in this compound the Ruderman–Kittel–Kasuya–Yosida (RKKY) exchange interaction mediated by the conduction electrons is expected to be absent, but the superexchange interaction reflecting the

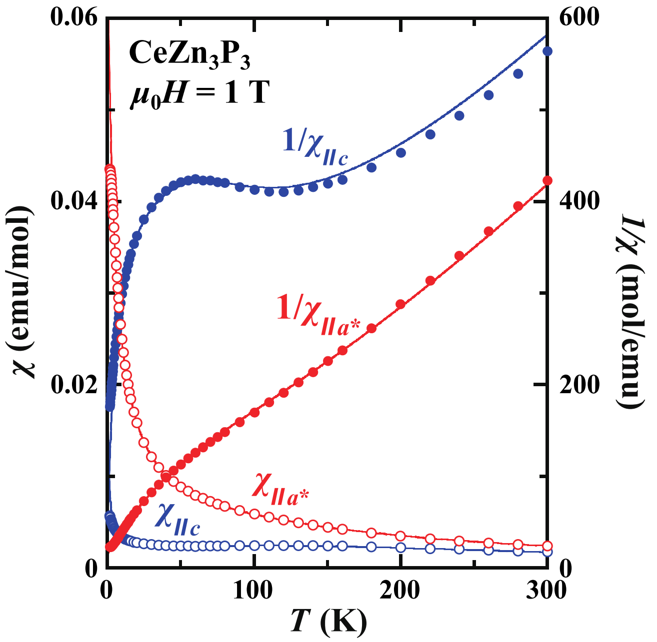

FIG. 2. Temperature dependencies of the magnetic susceptibilities ($\chi_{\parallel a^*}$ and $\chi_{\parallel c}$) of $CeZn_3P_3$ and their inverses ($1/\chi_{\parallel a^*}$ and $1/\chi_{\parallel c}$). Solid curves are the results of fitting using the CEF model.

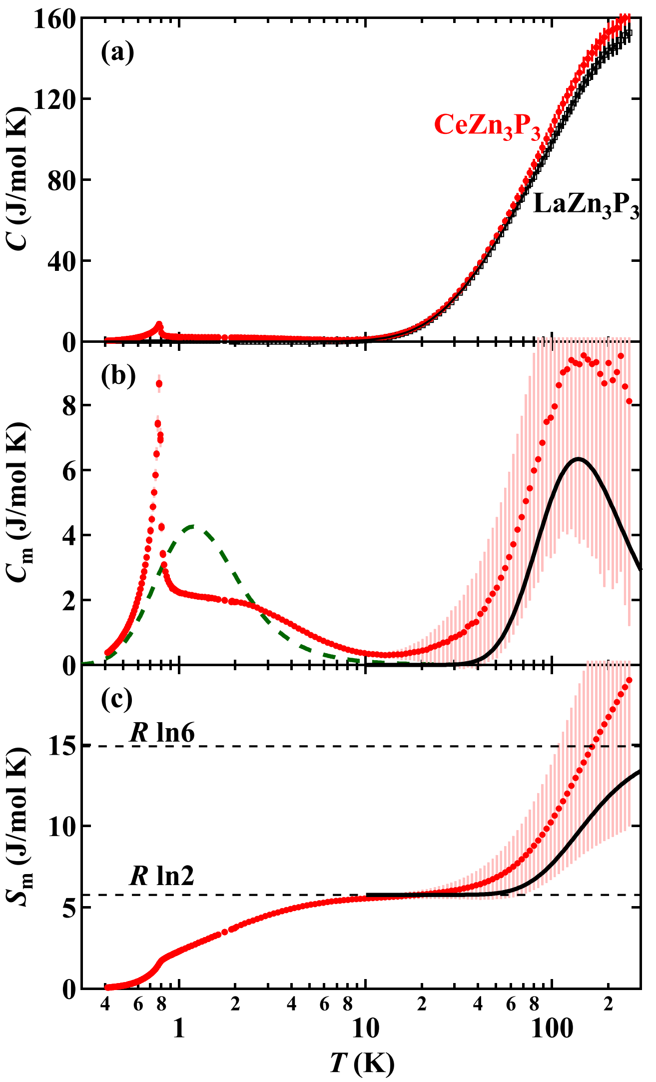

FIG. 3. (a) Specific heat (C) of $CeZn_3P_3$ (red closed circles) and that of $LaZn_3P_3$ (black open circles) in zero magnetic field. (b) Magnetic part of the specific heat of $CeZn_3P_3$ (C_m) in $\mu_0H = 0$ T as a function of the temperature. Red closed circles show $C_m = C_{CeZn_3P_3} - C_{LaZn_3P_3}$. The black solid curve is a result of the specific heat calculation using the CEF model, in which the same parameters as those used in the fitting for the magnetic susceptibilities are used. The dashed green curve below $T = 20$ K is a result of the specific-heat calculation using an isolated dimer model with the singlet-triplet splitting of $\Delta = 3.4$ K. (c) The associated magnetic entropy S_m estimated from C_m. The solid line is the entropy calculated by the CEF model plus $R \ln 2$ attributed to the ground-state Kramers doublet. The vertical bar in each panel represents the measurement error mainly due to a small amount of the samples.

geometrical arrangement certainly plays a much more important role than $YbAl_3C_3$ where a small amount of charge carriers are observed [12]. On the other hand, it may be crucially important in another sense that any sign of a phase transition is not detected down to 100 K in the temperature dependence of the resistivity in both $LaZn_3P_3$ and $CeZn_3P_3$.

Figure 2 shows the temperature dependence of the magnetic susceptibilities $\chi_{\parallel a^*}$ and $\chi_{\parallel c}$ of $CeZn_3P_3$ down to 1.8 K measured in a magnetic field 1 T along the a*axis and the c axis, respectively. $\chi_{\parallel a}$ measured in a magnetic field along the a axis is almost the same as $\chi_{\parallel a^*}$ and their difference is within the error bar. Their inverses ($1/\chi_{\parallel a^*}$ and $1/\chi_{\parallel c}$) are also shown. One order of magnitude larger values of $\chi_{\parallel a^*}$ than those of $\chi_{\parallel c}$ at low temperatures indicate an easy plane type anisotropy, which is probably ascribed to the CEF effect. Any sign of a phase transition could not be detected in the temperature range from 1.8 K to 300 K.

Figure 3(a) shows the temperature dependence of the specific heat of $CeZn_3P_3$ (red closed circles) and that of $LaZn_3P_3$ (black open circles) under zero magnetic field down to $T \approx 0.4$ K. A sharp peak of C of $CeZn_3P_3$ observed at $T_N = 0.8$ K certainly corresponds to a long-range antiferromagnetic order, as suggested by the kink of M_{a*}/H in the magnetization measurement described later. Except at $T_N = 0.8$ K of $CeZn_3P_3$, any sign of a phase transition was not detected up to $T \approx 250$ K in the specific-heat measurement for both samples under zero magnetic field. Figure 3(b) shows the temperature dependence of the magnetic part of the specific heat of $CeZn_3P_3$ (C_m). Red closed circles in this figure are obtained by subtracting the specific heat of $LaZn_3P_3$ from that of $CeZn_3P_3$, i.e., $C_m = C_{CeZn_3P_3} - C_{LaZn_3P_3}$. Above $T_N = 0.8$ K, the magnetic part of the specific heat shows a shoulder structure around $T \approx 3$ K and a long tail up to $T \approx 20$ K where the associated magnetic entropy S_m, which is estimated by integrating C_m/T, is close to $R \ln 2$ as shown in Fig. 3(c), although the entropy released up to T_N is only 30% of $R \ln 2$. These results imply that the magnetic ground state of $CeZn_3P_3$ is a Kramers doublet and or some sort of short-range order such as those originating from the geometrical frustration of the triangular lattice may effectively work. On the other hand, the broad peak structure around $T \approx 150$ K seen in C_m is considered to be attributed to the thermal excitation from the ground state to the CEF excited states, which may be several hundred kelvins above the ground state. The entropy S_m above 150 K exceeds $R\ln 6$, which is magnetic entropy expected from $2J{+}1$-fold degeneracy of the total angular momentum $J = 5/2$ of Ce^{3+} ion. However, it should be noted that the absolute values of the specific heat may have an error of a few percent for each sample since the weight of the sample used is at most a few mg. Therefore, this behavior is probably attributed to the measurement error because the value $R\ln 6$ remains in the error bar.

Next, to examine the magnetic state of $\mathrm{CeZn_3P_3}$ using these experimental results, the CEF effect is analyzed. Here, we assume the c axis as a quantized z axis. Under the assumption that the local symmetry of Ce-ion site in $\mathrm{CeZn_3P_3}$ is $D_{3\,d}$, the CEF Hamiltonian ($H_\mathrm{cry}^\mathrm{tri}$) is given as follows:

$$H_\mathrm{cry}^\mathrm{tri} = B_2^0 O_2^0 + B_4^0 O_4^0 + B_4^3 O_4^3, \tag{3}$$

where B_l^m represent CEF parameters and O_l^m are Stevens operators [21,22]. $H_\mathrm{cry}^\mathrm{tri}$ lifts sixfold degeneracy of $J = 5/2$ multiplet, creating three Kramers doublets, of which the wave functions have the following forms,

$$|\pm m_1\rangle = a\left|\frac{5}{2}, \pm\frac{1}{2}\right\rangle \pm \sqrt{1-a^2}\left|\frac{5}{2}, \mp\frac{5}{2}\right\rangle, \tag{4}$$

$$|\pm m_2\rangle = \mp\sqrt{1-a^2}\left|\frac{5}{2}, \pm\frac{1}{2}\right\rangle + a\left|\frac{5}{2}, \mp\frac{5}{2}\right\rangle, \tag{5}$$

$$|\pm m_3\rangle = \left|\frac{5}{2}, \pm\frac{3}{2}\right\rangle. \tag{6}$$

The CEF susceptibility (χ_cry) is calculated using the above wave functions and $H_\mathrm{cry}^\mathrm{tri}$, including parameters a, B_2^0, B_4^0, and B_4^3. For fitting of the actual magnetic susceptibility, the molecular field contribution (λ) and the diamagnetic susceptibility of the ion core (χ_0) are introduced as additional parameters, and the following expression is used:

$$\chi = \frac{\chi_\mathrm{cry}}{1 - \lambda\chi_\mathrm{cry}} + \chi_0. \tag{7}$$

Here, it should be noted that $|\pm m_3\rangle$ cannot become a CEF ground state because the uniaxial anisotropy of $|\frac{5}{2}, \pm\frac{3}{2}\rangle$ is not appropriate for the actual magnetic susceptibility, i.e., the easy-plane type anisotropy. Fitting results are shown by solid lines in Fig. 2. Calculated susceptibilities well reproduce the experimental results above $T \approx 5$ K, and obtained parameters are summarized in Table I.

To check the validity of the parameters obtained, the specific heat ascribed to the thermal excitation from the ground state to the CEF excited states is calculated using the CEF energy levels obtained by the fitting. The calculated specific heat and entropy are shown in Figs. 3(b) and 3(c) by solid curves. The peak temperature of C_m is well reproduced by the calculation whereas the absolute values are different. We stress that both curves remain in the experimental uncertainty. As the exited CEF levels locate more than 300 K higher than that of the ground state as understood from Table I, a well-isolated ground state is realized. Therefore, physical properties at low temperatures are mostly governed by the Kramers doublet ground state. Using the wave functions obtained, the magnetic anisotropy of the ground-state doublet is estimated as $g_J\langle J_z\rangle\mu_\mathrm{B} = \pm 0.196\mu_\mathrm{B}$ and $g_J\langle J_x\rangle\mu_\mathrm{B} = \pm 0.977\mu_\mathrm{B}$. A five times larger value of $g_J\langle J_x\rangle\mu_\mathrm{B}$ than that of $g_J\langle J_z\rangle\mu_\mathrm{B}$ indicates the easy-plane type magnetic anisotropy of $\mathrm{CeZn_3P_3}$. If we assume an effective spin $S = \frac{1}{2}$ corresponding to the Kramers doublet ground state, anisotropic g factors are defined as $g_{\parallel c} = 0.393$ and $g_{\perp c} = 1.95$.

TABLE I. Parameters used for the fitting of χ of $\mathrm{CeZn_3P_3}$ measured in $\mu_0 H = 1$ T in Figs. 2, 4(a), and 4(b).

CEF parameters		
B_2^0(K)	B_4^0(K)	B_4^3(K)
7.78	−0.784	16.5
Energy levels and wave functions		
	E(K)	Wave functions
$\|\pm m_1\rangle$	0	$0.87\,\|\frac{5}{2}, \pm\frac{1}{2}\rangle \pm 0.493\,\|\frac{5}{2}, \mp\frac{5}{2}\rangle$
$\|\pm m_2\rangle$	365	$\mp 0.493\,\|\frac{5}{2}, \pm\frac{1}{2}\rangle + 0.87\,\|\frac{5}{2}, \mp\frac{5}{2}\rangle$
$\|\pm m_3\rangle$	370	$\|\frac{5}{2}, \pm\frac{3}{2}\rangle$
Molecular field and diamagnetism		
λ_{a^*}(mol/emu)	λ_c(mol/emu)	χ_0(emu/mol)
−14.24	−22.39	−0.00024

To investigate the magnetic ground state and the interaction between them further, low-temperature parts of magnetic susceptibilities are examined. As stated before, it seems that the exchange interaction between the Kramers doublets may be generally isotropic, i.e., Heisenberg-type exchange interactions. In the case of $\mathrm{CeZn_3P_3}$, the dominant interaction is considered to be that in the Ce ion layer on the c plane, because the Ce ion layer is isolated by the layer composed of Zn and P ions from the next Ce ions layer by a distance of about 10 Å. Furthermore, there is no conduction electron that mediates the RKKY interaction. In the Appendix, according to Ref. [7] we introduce the exchange interaction between the first-nearest Ce ions on the c plane, where only the ground-state Kramers doublets are taken into account and the slight deformation of the crystal structure, which will be described later, is ignored. Under the above assumptions, the obtained result indicates that the exchange interaction is isotropic.

In Figs. 4(a) and 4(b), magnetic susceptibilities and their inverses below $T = 10$ K of $\mathrm{CeZn_3P_3}$ are shown. Although no sign of the magnetic order is visible down to 1.8 K, $\chi_{\parallel a^*}$ in Fig. 4(a) is remarkably suppressed below $T \approx 5$ K, suggesting a short-range antiferromagnetic correlation arising from the geometrical frustration of the triangular lattice or some cause. To estimate the paramagnetic Curie temperature (Θ_p), which is considered to be comparable to the strength of the exchange interaction, we notice the low-temperature part of the inverse susceptibilities. Here, we would like to point out that the estimation of Θ_p from $1/\chi$ above several ten kelvins often leads to incorrect results in $4f$-electron magnets, because χ in such a temperature region is usually strongly affected by the CEF splitting. A broad peak of $1/\chi$ of $\mathrm{CeZn_3P_3}$ around $T \approx 50$ K is certainly ascribed to the thermal excitation from the CEF ground state to the CEF excited states

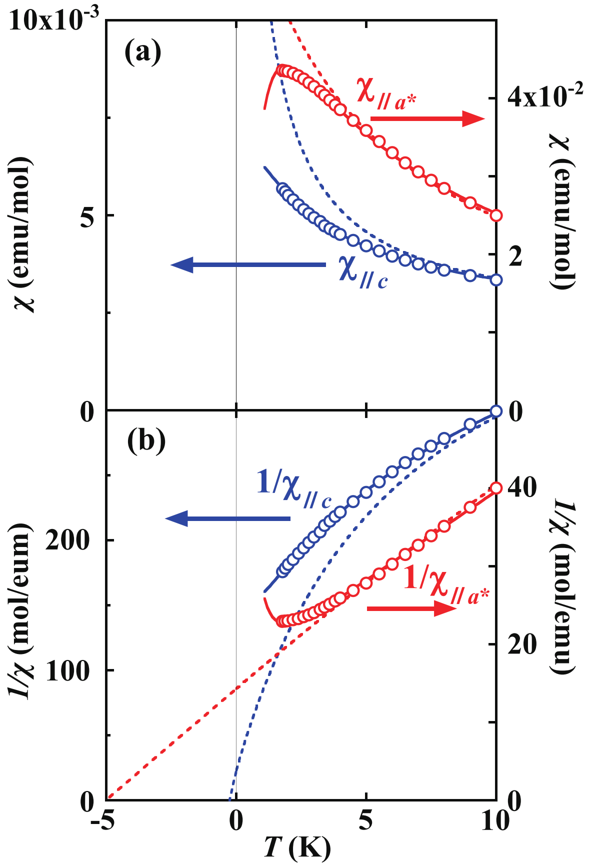

FIG. 4. Low-temperature part of (a) $\chi_{\parallel a^*}$ and $\chi_{\parallel c}$ and (b) their inverses of CeZn$_3$P$_3$ measured in the field $\mu_0H = 1$ T. Dotted curves are results of fitting using the CEF model. Dotted lines in the negative temperature region are their extrapolations, which cross the horizontal axis at about -5 K and -0.3 K. Solid curves are results of fitting using the interacting dimer model described later.

as reproduced by the CEF model. Therefore, Θ_p of the ground state should be estimated from a low-temperature part of $1/\chi$ obeying the Curie-Weiss law. On the other hand, we should also notice that $1/\chi_{\parallel a^*}$ below $T \approx 5$ K is strongly affected by the short-range antiferromagnetic correlation. Considering the above-mentioned aspects, Θ_p along the a^* axis is estimated to be $-6 \sim -7$ K from the extrapolation of $1/\chi_{\parallel a^*}$ in the temperature range of $5\text{ K} \lesssim T \lesssim 10$ K. In contrast to $1/\chi_{\parallel a^*}$, $1/\chi_{\parallel c}$ has no definite region where $1/\chi_{\parallel c}$ is proportional to the temperature, so a similar procedure as that for $1/\chi_{\parallel a^*}$ is inadequate to estimate Θ_p along the c axis.

To overcome this problem, the result of the susceptibility fitting using the CEF model is useful because it well reproduces the magnetic susceptibility in the temperature range above 10 K where the short-range antiferromagnetic correlation can be ignored. By extrapolating the fitting curves to negative temperature range as shown by dotted lines in Fig. 4(b), Θ_p are estimated to be about -5 K along the a^* axis, which is almost comparable to that estimated above, and about -0.3 K along the c axis.

In the flame of the mean-field approximation, Θ_p corresponds to the strength of the exchange interaction along each direction. Therefore, when the Hamiltonian of Eq. (1) is adequate for CeZn$_3$P$_3$, $(g_z/g_x)^2$ is expected to be 0.06, which is close to $(g_{\parallel c}/g_{\parallel a^*})^2 = 0.038$ obtained from the CEF analysis. Therefore, if the estimation of Θ_p is correct, this result suggests that the exchange interaction in CeZn$_3$P$_3$ is anisotropic, probably reflecting anisotropic wave function, although it contradicts the results in the Appendix. We will discuss this problem again later.

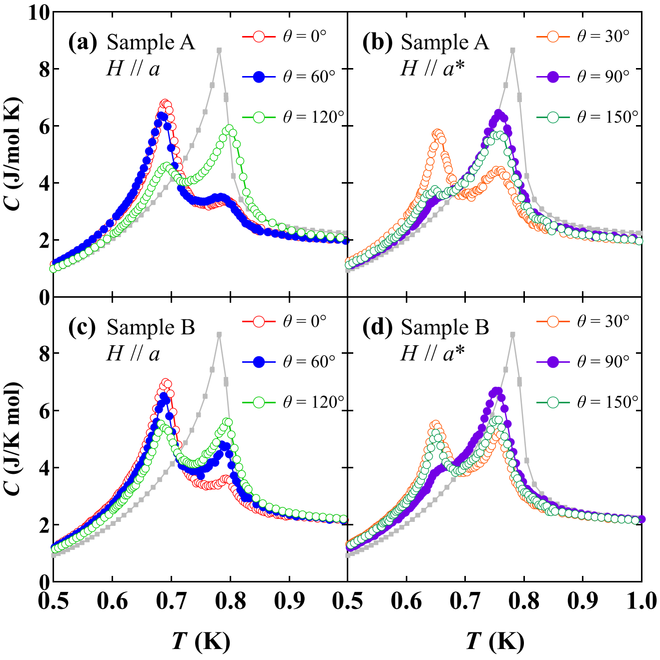

FIG. 5. Temperature dependence of specific heat (C) of CeZn$_3$P$_3$ single crystal under the magnetic field $\mu_0H = 1$ T for two different single crystals A and B at zero-magnetic field. Square gray marker shows zero-field C of single crystals used in Fig. 3. The magnetic field is applied along three directions of the a axis ($\theta = 0°$) and its equivalent directions of $\theta = 60°$ and $120°$ in (a) sample A and (c) sample B, and along three directions of the a^* axis ($\theta = 90°$) and its equivalent directions of $\theta = 30°$ and $150°$ in (b) sample A and (d) sample B, where θ is the angle between the a axis and the magnetic field.

B. Sample-dependent specific heat of CeZn$_3$P$_3$ under magnetic field

As said in the previous subsection, the magnetic phase transition of CeZn$_3$P$_3$ at $T_N = 0.8$ K is observed as a single sharp peak of C. By applying a magnetic field, this sharp peak of C splits as shown in Figs. 5(a)–5(d), where the temperature dependencies of C of a CeZn$_3$P$_3$ single crystal under the magnetic field $\mu_0H = 1$ T are shown for different samples A and B. We also plot C in Fig. 3 to compare with that under the field. Note that the zero-field specific heat is sample independent. The magnetic field is applied along the a axis ($\theta = 0°$) and its equivalent directions of $\theta = 60°$ and $120°$ in Figs. 5(a) and 5(c), and the a^* axis ($\theta = 90°$) and its equivalent directions of $\theta = 30°$ and $150°$ in Figs. 5(b) and 5(d), where θ is the angle between a certain a axis and the magnetic field in the c plane. Common to these figures, two peaks of C are always observed at almost the same temperatures of $T \approx 0.69$ K and $T \approx 0.8$ K for $H \parallel a$ axis in Figs. 5(a)

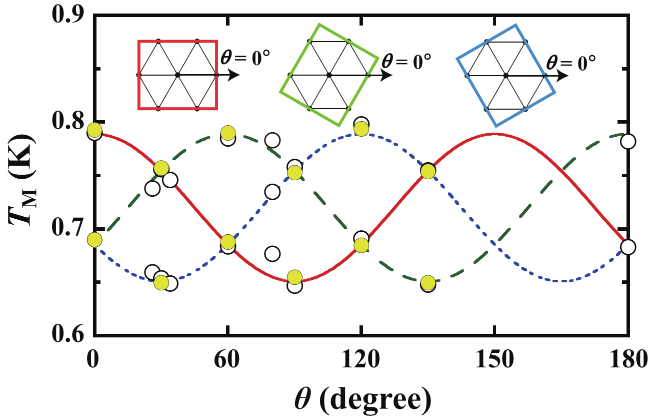

FIG. 6. Magnetic field angle (θ) dependence of transition temperature (T_M) of $CeZn_3P_3$ under the magnetic field $\mu_0H = 1$ T for two different single crystals A (black open circle) and B (yellow closed circle), where θ is the angle between the a axis and the magnetic field in the c plane. All points are roughly reproduced by three curves with phases shifted by 60° (solid, dotted, and broken curves) represented by $T_M = 0.069\cos(2\theta) + 0.72$ K, $T_M = 0.069\cos(2\theta + 60°) + 0.72$ K and $T_M = 0.069\cos(2\theta + 120°) + 0.72$ K. Here, rather than specific functional form, it is important that three functions with the same symmetry coexist. Three kinds of structural domains are also shown.

and 5(c) and $T \approx 0.65$ K and $T \approx 0.75$ K for $H \parallel a^*$ axis in Figs. 5(b) and 6(d), although their peak heights distinctly change, depending on the sample. Furthermore, their peak heights depend on the field direction even though they are in the equivalent direction. In addition, the following facts are confirmed concerning C:

(1) There is no difference between results measured after zero-field cooling and field cooling.

(2) The specific heat shows good reproducibility even once after having heated the sample to room temperature.

(3) The peak never splits by the application of the magnetic field along the c axis up to $\mu_0H = 15$ T.

First, we can point out a symmetry breaking for the c plane. In addition to this, the above issues (1) and (2) indicate this symmetry breaking is not accompanied by the magnetic transition but possibly the structural transition. Therefore, one may think that these peaks may be attributed to the magnetic transitions but its basement is in the symmetry breaking for the hexagonal crystal structure, i.e., a structural phase transition. Furthermore, we could not detect any anomaly suggesting the structural phase transition up to room temperature by the electrical resistivity [20], the magnetic susceptibility, and the specific-heat measurement. Therefore, it may be either that the structural phase transition occurs at a higher temperature than room temperature or that the crystal structure is not hexagonal in the first place. Here, we should note again that these behaviors are sample dependent. This means that the resultant structure of the structural transition is not uniform but possibly consists of multiple domains.

These results mentioned so far remind us of $YbAl_3C_3$ with the same $ScAl_3C_3$ structure. $YbAl_3C_3$ shows the structural phase transition from the hexagonal structure to the orthorhombic one at $T \approx 80$ K [11,12], which is caused by very slight displacement of constituent elements and cannot be detected by the neutron powder diffraction measurement, similar to the result of the present x-ray powder diffraction [23]. Here it is noted that the orthorhombic deformation occurs along three equivalent a-axis directions, then the multidomain structure consisting of three kinds of orthorhombic domains appears in $YbAl_3C_3$ [24]. If similar deformation emerges in $CeZn_3P_3$, two peaks of C are interpreted as the magnetic transitions of each domain group because magnetic responses of three kinds of domains in both field directions along a and a^* axes are classified to two groups regarding the angle between the field direction and the principal axis. Here, we would like to point out that a similar crystal deformation was recently found in $CeCd_3P_3$ and $CeCd_3As_3$ of $CeZn_3P_3$ analog, although its details are still open question [25,26].

If our conjecture is correct, the following two matters should be satisfied. One is twofold rotational symmetry around the c axis reflecting orthogonal symmetry, and the other is that three kinds of the twofold rotational symmetry coexist, reflecting the three kinds of structural domains. In fact, these are confirmed in Fig. 6, where the magnetic transition temperatures (T_M) of the C peaks are plotted as a function of the angle (θ) between a certain a axis and the field direction. Observed T_M are roughly reproduced by three trigonometric functions, which are functional forms for convenience and in reality seem to be a bit more complicated, with a period of angle 180° and with the phase angle shifted by 60°. These angles are equivalent to twofold rotational symmetry around the c axis and three kinds of twofold rotational symmetry, respectively. Three types of domains are also symbolically represented in Fig. 6.

At the present stage, we can conclude that the crystal structure of $CeZn_3P_3$ is possibly orthorhombic and not the hexagonal $ScAl_3C_3$ type definitely, and that a multidomain structure composed of three types of domains is formed. But as said before, since it is rather difficult to detect its deformation by ordinary x-ray powder diffraction, the deformation may be extremely small. So, its crystal structure could be treated as an almost hexagonal one at the zeroth approximation.

C. Thermal properties of $CeZn_3P_3$ under magnetic field at low temperatures

1. *Field dependence of magnetocaloric effect of* $CeZn_3P_3$ *on the c plane at low temperatures*

Just as the transition temperature in the magnetic field is different for each structural domain, the transition field is also expected to be different for each structural domain. To separate the transition magnetic field of each domain, it is sufficient to examine the magnetic field angle dependence as in the previous section. For this purpose, the measurement of the MCE was performed at low temperatures for the $H \parallel c$ plane, sweeping the magnetic field up and down at a constant speed. In this MCE measurement, only one sample that looks like a single crystal as shown in Fig. 1(b) is used. The quasiadiabatic condition of the MCE measurement requires a sharp change in the sample temperature when crossing a phase transition or crossover point to ensure entropy conservation. The typical experimental result of the MCE measurement is

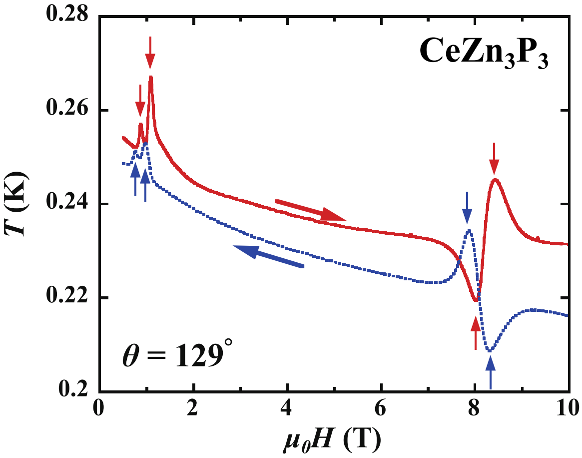

FIG. 7. The magnetic field dependence of the sample temperature obtained by the MCE measurement. The magnetic field is applied to the c plane and its angle with the a axis (θ) is 129°. Vertical arrows may indicate a phase transition or crossover point.

shown in Fig. 7, where the horizontal axis is the magnetic field and the vertical axis is the sample temperature. Therefore, the position of the top of the peak or the bottom of the valley may correspond to the point of the phase transition or the like, as shown by arrows. Here, the two peaks in the low field region of $\mu_0H \approx 1$ T only slightly change in position when the magnetic field is raised or lowered; however, the peaks and valleys in the high field region of $\mu_0H \approx 8$ T are reversed by raising and lowering the magnetic field.

First, to pick up the signal from each domain, the field dependencies up to 3 T of the sample temperature are shown in Fig. 8(a) for various angles (θ) between a certain a axis and the magnetic field direction on the c plane. All data points in Fig. 8(a) were obtained when raising the magnetic field. Reverse triangle marks indicate the peak position, and their size the peak height. It is evident that different height peaks are present, suggesting different signals from the majority domain and the minority domain. Peak positions in Fig. 8(a) are converted to the phase boundary in magnetic field strength (μ_0H) versus magnetic field direction (θ) phase diagram of Fig. 8(b), where higher peaks are represented by larger black circles. As shown in Fig. 8(b), by connecting the larger black circles, a phase of the majority domain extending from about 30° to about 150° could be determined. A black solid curve presents a phase boundary. By similar procedure, another two phases, of which boundaries are shown by the blue dashed curve and the green dotted curve, are identified. These phases are well understood, assuming three structural domains as suggested by the specific-heat measurement under the magnetic field because there are three kinds of twofold rotational symmetry. The fact that the two boundaries do not affect each other when they intersect also suggests that the boundaries are independent of each other, i.e., independent of different domains. From this phase diagram, it is also understood that two peaks near 1 T in Fig. 7 originate from the same phase boundary in different domains. On the other hand, the reason why the two peaks near 1 T change their positions slightly by raising or lowering the magnetic field is that this is a first-order phase transition as understood by the magnetization measurement described later.

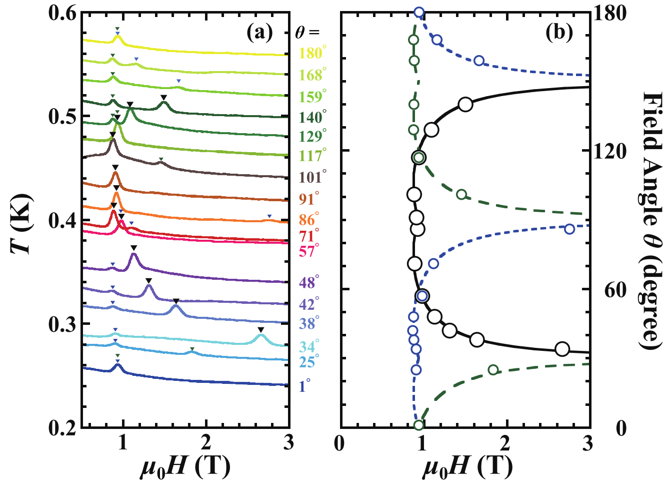

FIG. 8. (a) The magnetic field dependencies of the sample temperature for various angles (θ) between certain a axis and the magnetic field direction on the c plane obtained by the MCE measurement. Reverse triangle marks indicate the peak position, and their size the peak height. The origin of the vertical axis for each curve is shifted by 0.02 K sequentially from the curve of 1°. (b) Magnetic field versus θ phase diagram at $T \approx 0.25$ K created based on the result of (a). There are three kinds of phases due to different domains, one of which extends from about 30° to about 150° as shown by the black solid curve.

In contrast to the low field phase boundaries, the high field phase boundaries appear to reflect hexagonal symmetry rather than twofold symmetry. Figure 9(a) shows the magnetic field dependence of the sample temperature in the field between

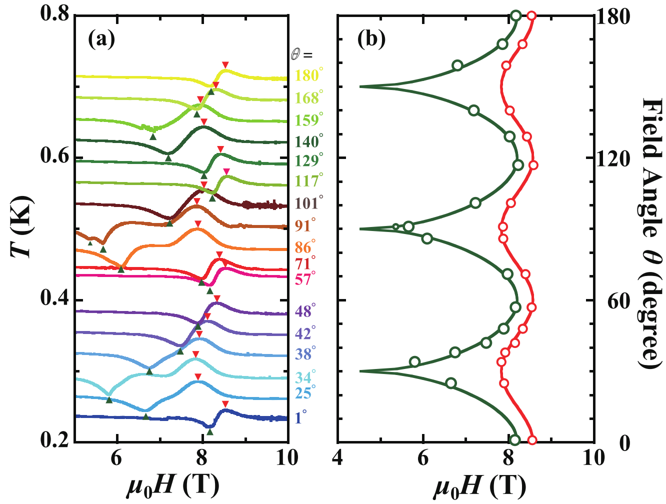

FIG. 9. (a) The field dependencies of the sample temperature for various angles (θ) between certain a axis and the magnetic field direction on the c plane. Reverse and normal triangle marks indicate the top of the peak and the bottom of the valley. The origin of the vertical axis for each curve is shifted by 0.03 K sequentially from the curve of 1°. (b) Magnetic field versus θ phase diagram at $T \approx 0.25$ K obtained from MCE measurement.

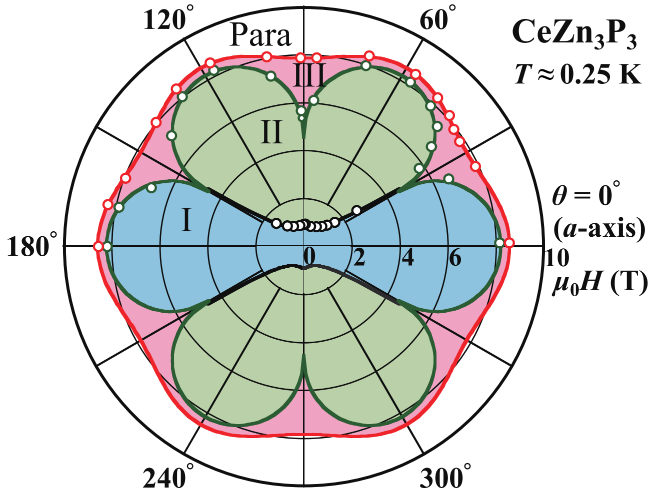

FIG. 10. H-θ phase diagram of the majority domain of $CeZn_3P_3$ at $T \approx 0.25$ K. Here $\theta = 0°$ corresponds to the a axis of the orthorhombic structure of the majority domain. $\theta = 90°$ corresponds to the b axis of the majority domain in the orthorhombic structure and a^*axis in the hexagonal structure. There are three magnetic phases of I–III plus para (induced-ferro) magnetic phase. In the actual sample, this phase diagram overlaps with that shifted by 60° and that shifted by 120°.

5 T and 10 T for various angles (θ) between a certain a axis and the magnetic field direction on the c plane. All data points in Fig. 9(a) were obtained when raising the magnetic field. Reverse and normal triangle marks indicate the top of the peak and the bottom of the valley, respectively. It is evident that the heights of the peaks are almost the same as well as the depths of the valleys in contrast to those of the low field phase boundaries, except for the $\theta = 91°$ curve where an additional small valley is observed at around 5.4 T. The peak and valley positions in Fig. 9(a) are converted to phase boundaries in $\mu_0 H$ vs θ phase diagram of Fig. 9(b). From this figure, it is clear that (1) There are two types of phase boundaries corresponding to the peak or valley of the MCE curve when raising the magnetic field and (2) both phase boundaries have sixfold symmetry. These results suggest that a magnetic field with sufficient strength overcomes the effect of the slight structural deformation, resulting in the emergence of the almost sixfold rotational symmetry. It becomes clearer when making a phase diagram as a function of the field direction and strength.

Figure 10 shows a magnetic phase diagram of the majority domain of $CeZn_3P_3$ at $T \approx 0.25$ K related to the dependence of magnetic field strength and direction on the c plane. To draw this phase diagram, we used the solid line of $\theta = 30°$ to 150° in Fig. 8(b), i.e., the boundary of the majority domain, and all the boundary lines in Fig. 9(b), and then applied the twofold symmetry to them. By combining this phase diagram and three kinds of structural domains that differ from each other by 60° or 120°, the results in Figs. 8 and 9 can be consistently explained. As understood from Fig. 10, three magnetic phases of I–III plus para (induced-ferro) magnetic phases appear. As said before, phase boundaries at the high magnetic field region reflect the original symmetry of sixfold symmetry. The relation of the magnetic field strength and direction on the boundary between phase III and the para phase is well expressed by the following equation assuming a simple form:

$$\mu_0 H = 0.37\cos(6\theta) + 8.2 \quad \text{T}. \tag{8}$$

Red solid curves in Figs. 9(b) and 10 are drawn by this equation with sixfold symmetry. On the other hand, assuming a simple form, the boundary between phase III and phase I or II is represented by the following equation with sixfold symmetry:

$$\mu_0 H = 3.66\sqrt{|\cos(3\theta)|} + 4.54 \quad \text{T}. \tag{9}$$

This equation also well reproduces the boundary as shown by green solid curves in Figs. 9(b) and 10. In contrast to these boundaries, the boundaries between phase I and phase II reflect a twofold symmetry. The solid black line extending from $\theta = 30°$ to 150° in Fig. 8(b) is created by connecting the following two curves at $\theta = 90°$:

$$\mu_0 H = \frac{0.87}{\sqrt{\cos(2(\theta - 75))}} \quad \text{T}, \tag{10}$$

$$\mu_0 H = \frac{0.87}{\sqrt{\cos(2(\theta - 105))}} \quad \text{T}. \tag{11}$$

At the present stage, it is not clear why boundaries are represented by such a simple functional form, but its symmetry will be discussed later.

2. *Temperature dependence of specific heat and magnetocaloric effect of* $CeZn_3P_3$ *at low temperatures*

Phase boundary that depends on the direction of the magnetic field will also depend on the temperature. In addition to the MCE measurement at various temperatures, we measured the temperature dependence of C under the magnetic field of various strengths and directions using the same sample used in the MCE measurement. Figures 11(a) and 11(b) show temperature dependencies of C under several selected magnetic fields with field angles $\theta = 57°$ and 180° on the c plane, respectively. Here, the field angle θ is the same as that of the phase diagram in Fig. 10, but only that of the majority domain is drawn in Fig. 10.

Therefore, to ensure an accurate interpretation of the specific heat, we reconfirm the complicated situation due to the domain structure of $CeZn_3P_3$. Since $CeZn_3P_3$ is composed of three structural domains whose angles are different from each other by 60°, the experimental result of C of $\theta = 57°$ in Fig. 11(a) also includes contributions of C from the minority domains which correspond to $\theta = 117°$ and $\theta = 177°$. Here, we should note that the contribution from C of $\theta = 117°$ is thought to overlap almost completely with that of $\theta = 57°$ as deduced from Fig. 10. So, it is thought that only the peak of $\theta = 177°$ is observed independently, which probably corresponds to the minor peak in $\mu_0 H = 1$ T observed at a higher temperature side than that of the major peak in Fig. 11(a).

Similarly, C of $\theta = 180°$ in Fig. 11(b) also includes contributions of C of $\theta = 120°$ and 60° from the minority domain, which are thought to overlap and appear to be observed independently of the major peak, and probably correspond to minor peaks on the lower temperature side observed in $\mu_0 H = 1$ T and 2 T. Here, we recall that $\theta = 57°$ is very

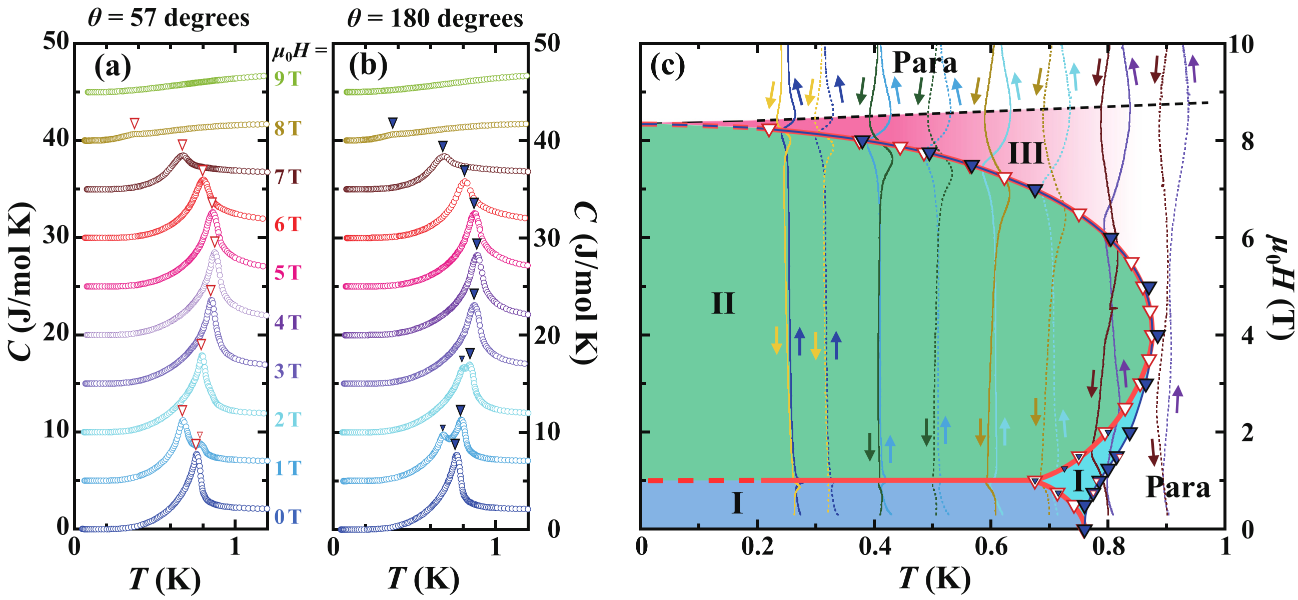

FIG. 11. Temperature dependence of C of $\mathrm{CeZn_3P_3}$ in several selected magnetic fields along the c plane with (a) $\theta = 57^\circ$ and (b) $\theta = 180^\circ$ with regard to the majority domain. Reverse triangle marks indicate the peak positions. (c) H-T phase diagram of $\mathrm{CeZn_3P_3}$ drawn by collecting the peak positions of C and MCE measurement. Large red open triangles are major peaks of C with $\theta = 57^\circ (\approx 60^\circ)$ and small one are minor peaks. Large blue closed triangles are major peaks of C with $\theta = 180^\circ$ and small one are minor peaks. Results of MCE measurements at several selected temperatures are also shown. Solid curves are measured in the magnetic field with $\theta = 57^\circ (\approx 60^\circ)$ and dotted curves are measured in those with $\theta = 180^\circ$. The direction of the arrow corresponds to the increase or decrease of the magnetic field.

close to 60°. In fact, as shown in Fig. 10, it seems that there is almost no difference between these two, and it becomes clear in Fig. 11(c).

By summarizing the peak positions of C, which are specified by the inverted triangles, under the magnetic fields in Figs. 11(a) and 11(b), the $H - T$ phase diagram of Fig. 11(c) is obtained. Red open and blue closed triangles represent peaks of C with $\theta = 57^\circ$ and 180°, respectively. Whether the size of the triangle is large or small corresponds to the major peak or the minor peak. The major peak of $\theta = 57^\circ$ overlaps with the minor peak of 180° and vice versa. This means that the red thick solid curve determined from the large red open and small blue closed triangles in Fig. 11(c) indicate the phase boundary along H parallel to $\theta \approx 60^\circ$ or $\theta \approx 120^\circ$. Similarly, the blue thin solid curve determined from the large blue closed and the small red open triangles indicates the phase boundary along H parallel to $\theta \approx 0^\circ$ or $\theta \approx 180^\circ$. That is, the phase diagram of Fig. 11(c) is a superposition of two phase diagrams in the $\theta = 0^\circ$ direction and the $\theta = 60^\circ$ direction.

In contrast to the smooth curvature of the blue thin boundary, the red thick boundary is sharply bent at approximately 1 T. It probably indicates the boundary between phase I and II in Fig. 10 starting from this bending point. In fact, peaks or valleys observed around 1 T in the MCE measurement at various temperatures indicate the boundary between phase I and phase II in Fig. 11(c), where solid curves are measured in the magnetic field with $\theta = 57^\circ (\approx 60^\circ)$ and dotted curves are measured in those with $\theta = 180^\circ (= 0^\circ)$. The direction of the arrow corresponds to the increase or decrease of the magnetic field. Here, we should also note that the peaks or valleys of MCE curves correspond to the boundary drawn by collecting the peak of C. Therefore, the solid curve around 8 T corresponds to the boundary between phases II and III. On the other hand, the peaks and valleys in the range between 8 T and 9 T in the MCE curves are considered to correspond to a boundary between phase III and the para phase (induced ferromagnetic phase), as can be seen from Fig. 10. These peaks and valleys become wider and obscure with increasing temperature. We could not find a clear anomaly in the specific heat for this boundary. This is probably because the boundary line is close to parallel to the horizontal axis (temperature axis) or because it is a crossover rather than a phase transition. Since this boundary seems to slowly fade away with temperature, judging from the MCE curves, it is considered to be a crossover at least on the high-temperature side. Therefore, the higher temperature side of phase III is not closed. Here we should note that phase III at absolute zero is almost absent on the $\theta = 0^\circ$, 60°, and 120° lines as predicted from Fig. 10.

The procedure described above applies to the results under magnetic fields with different directions. Figure 12(a) shows temperature dependencies of C under several selected magnetic fields with a field angle $\theta = 86^\circ$ on the c plane, where peaks corresponding to the phase transition are clearly observed. As well as the case of $\theta = 57^\circ$ and $\theta = 180^\circ$ in Figs. 11(a) and 11(b), the experimental result of C of $\theta = 86^\circ$ in Fig. 12(a) includes contributions of C from the minority domains, which corresponds to $\theta = 86^\circ \pm 60^\circ$, i.e., 26° and 146°. The point to note here is that $\theta = 86^\circ$ is close to 90°, but not exactly the same as 90°. As deduced from Fig. 10, the phase transition between phase I and phase II occurs at approximately 1 T for both $\theta = 86^\circ$ and 146°. Therefore, the C peaks of $\theta = 146^\circ$ are thought to overlap with those of $\theta = 86^\circ$ and they will be observed as one peak. On the other hand, phase II does not appear in the case of $\theta = 26^\circ$. Therefore, the peak of $\theta = 26^\circ$ may be observed independently, which probably corresponds to the minor peak in 1 T

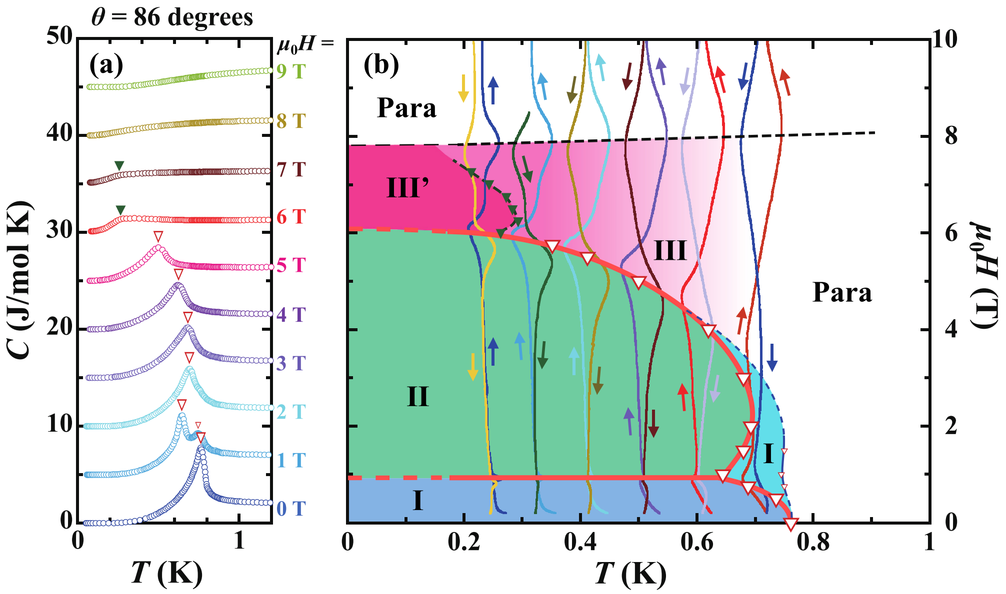

FIG. 12. (a) Temperature dependence of C of $\mathrm{CeZn_3P_3}$ in several selected magnetic fields along the c plane with $\theta = 86^\circ$ with regarding the majority domain. Reverse red open triangle marks indicate the peak positions of C and green open marks indicate the bending positions of C. (b) H-T phase diagram of $\mathrm{CeZn_3P_3}$ drawn by collecting the peak positions of C and MCE measurement. Large red open triangles are major peaks of C with $\theta = 86^\circ$ and small ones are minor peaks which are possibly due to those of $\theta = 26^\circ$. Results of MCE measurements at several selected temperatures are also shown. The direction of the arrow corresponds to the increase or decrease of the magnetic field.

observed at a higher temperature side than that of the major peak. It should also be noted that bends of C specified by the green closed inverted triangles were observed in the range 6 T $< \mu_0 H <$ 8 T in addition to the C peaks specified by red open triangles observed below 5 T. These are not considered to be normal phase transitions, but some changes in circumstances such as crossover are expected.

By summarizing the peak and bend positions of C under the magnetic fields in Fig. 12(a), the $H - T$ phase diagram of Fig. 12(b) is obtained. Red large open and small closed triangles correspond to the major and minor peaks of C, respectively. The results of the MCE measurement are also shown here. A thick phase boundary determined from the large red open triangles is sharply bent at approximately 1 T, probably indicating the boundary from phase I to II in Fig. 10 as well as Fig. 11(c). In fact, peaks or valleys observed around 1 T in the MCE measurement at various temperatures indicate the boundary between phase I and phase II in Fig. 12(b) while the boundary represented by the thin solid curve is obtained by collecting red open triangles, which corresponds to the minor peaks of C in Fig. 12(a). This is the contribution from minority domains of $\theta = 26^\circ$, where the boundary between I and II is absent. Here, we should also note that the peaks or valleys of MCE curves other than near 1 T coincide with the boundary drawn by the red large open triangles collecting the major peak of C. Therefore, the red solid thick curve below about 6 T corresponds to the boundary between phases II and III.

On the other hand, the peaks and valleys around 8 T in the MCE curves are considered to correspond to a boundary between phase III and the para phase (induced ferromagnetic phase), as can be seen from Fig. 10. Unlike the case of the magnetic field along $\theta = 57^\circ$ or 180°, as seen in Fig. 11(c), phase III occupies a finite magnetic field region even at absolute zero temperature in Fig. 12(b). In addition, phase III below 0.2 ~ 0.3 K and that above it seem to be separated by the bending of the specific heat, as indicated by green closed triangles. However, at the present stage, no clear difference has been observed in the physical properties of these two regions, so the low-temperature phase is referred to as phase III′ for convenience, corresponding to the high-temperature phase being referred to as phase III.

By the C and MCE measurements under magnetic fields in various directions, many phase diagrams similar to the phase diagram of Fig. 10 in various temperatures were obtained. Similarly, many $H - T$ phase diagrams such as Figs. 11(c) and 12(b) can be drawn for many field directions by the C and MCE measurements. Summarizing this information, we can obtain the three-dimensional phase diagram shown in Fig. 13, which includes the strength and direction of the magnetic field and the temperature. The magnetically ordered state, which is divided into two regions, has an uneven dome shape and is surrounded by an unclear state, of which character will be discussed later.

D. Magnetic properties of $\mathrm{CeZn_3P_3}$ at low temperatures

1. Magnetization of $\mathrm{CeZn_3P_3}$ *at low temperatures*

To directly examine the magnetic state, the magnetization measurement below 1.8 K was performed by the Faraday balance method using a superconducting magnet. In this experiment, multiple $\mathrm{CeZn_3P_3}$ crystals aligned and stacked together were used to improve the accuracy of magnetization.

Figure 14(a) displays the temperature dependence of the magnetization along the a^* axis divided by the magnetic fields along the a^* axis (M_{a^*}/H) for several magnetic fields. In low magnetic fields up to 4 T, the M_{a^*}/H curves form broad peaks and then show kinks with decreasing temperature. These broad peaks of M_{a^*}/H seem to link to the suppression

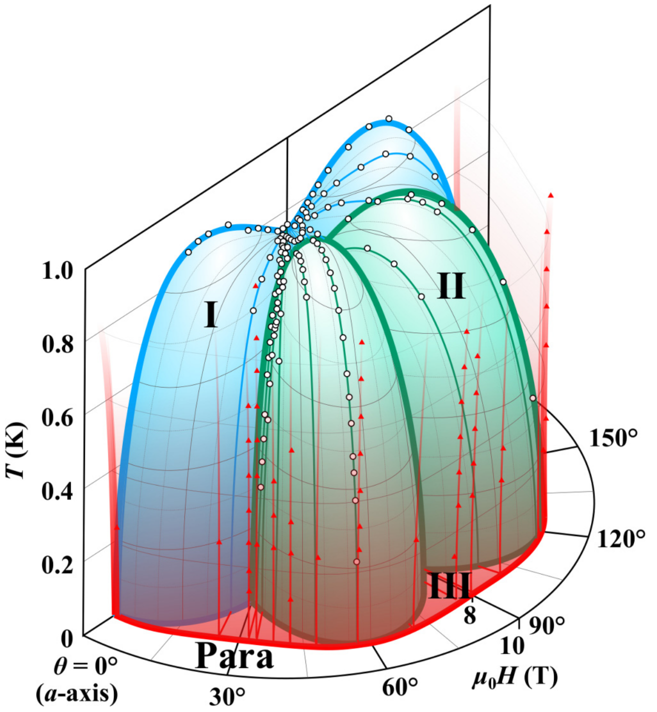

FIG. 13. Three-dimensional magnetic field-temperature phase diagram that incorporates the magnetic field orientation.

of $\chi_{\parallel a^*}$ in Fig. 4(a) and suggest the short-range antiferromagnetic correlation ascribed to the geometrical frustration of the triangular lattice, or otherwise the formation of dimers as seen in $\mathrm{YbAl_3C_3}$ [9,11]. On the other hand, the kinks of M_{a^*}/H possibly indicate the long-range antiferromagnetic order, i.e., T_N. Here, it is necessary to pay attention to the direction of the magnetic field. As mentioned above, the sample used is a stack of multiple aligned crystals. In addition, each crystal is composed of three structural domains. Therefore, the a^* direction means that the three directions ($\theta = 30°$, $90°$, and $150°$) in Fig. 10 are included. In the case of $H = 0.75$ T, when the temperature is reduced from the paramagnetic phase, all regions of $\theta = 30°$, $90°$, and $150°$ fall into phase I as expected from Fig. 10, although the transition temperatures of each region are slightly different from each other. On the other hand, in the case of $\mu_0 H = 2.5$ T and 4 T, when the temperature is lowered, some regions change to phase I and others change to phase II. The actual experimental results are a superposition of these two cases. In any case, in the magnetic field region of this degree, $\mathrm{CeZn_3P_3}$ undergoes a phase transition to a long-range magnetically ordered state with decreasing temperature, and the approximate transition temperature is indicated by arrows in Fig. 4(a). When the magnetic field is raised to 6 T, it seems that the transition to the ordered state no longer occurs down to $T \approx 0.5$ K. This is probably because this magnetic-field region corresponds to phase III, which is an unclosed region. Here, it is also noted that M_{a^*}/H in the paramagnetic region totally increases with increasing field. This trend suggests that M versus H curve has an upward curvature, as discussed later.

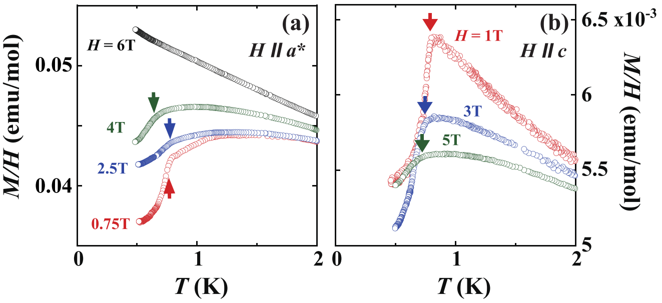

FIG. 14. (a) The temperature dependence of the magnetization of $\mathrm{CeZn_3P_3}$ divided by the magnetic fields along the a^* axis (M_{a^*}/H). Vertical arrows indicate a long range antiferromagnetic order. (b) The temperature dependence of the magnetization divided by the magnetic fields along c axis (M_c/H).

When the magnetic field is applied along the c axis, the magnetization divided by the magnetic field (M_c/H) shows the kink corresponding to the antiferromagnetic order, i.e., T_N, as shown in Fig. 14(b), but the broad peak is almost invisible under low magnetic fields around $\mu_0 H = 1$ T in contrast to the case of the field being parallel to the a^* axis. Also, in contrast to the case of the field being parallel to the a^* axis, T_N does not saturate at the strength of the applied magnetic field, which is also supported by the specific-heat measurement although it is not shown. A further contrast to the case of the magnetic field applied along the a^* axis is that the magnitude of M/H in the paramagnetic region decreases with increasing magnetic field.

Figure 15(a) shows magnetization isotherms at several temperatures below 1.8 K in magnetic fields along the a^* axis. Although the magnetization curves appear to increase monotonically with increasing magnetic field at first glance, those seem to have fine structures when examining those in detail. As shown by vertical arrows in Fig. 15(a), three small steps, i.e., discontinuous changes, and one bend, i.e., a continuous change, seem to exist. To clarify these structures, we differentiated M_{a^*} by H. Figure 15(b) shows the field derivative of the magnetization of $\mathrm{CeZn_3P_3}$ measured in $H \parallel a^*$ (dM_{a^*}/dH). Corresponding to the three steps of M_{a^*}, three peaks of dM_{a^*}/dH can be recognized, suggesting first-order phase transitions. Actually, the first magnetization step around $\mu_0 H = 0.9$ T shows a hysteretic behavior as shown in the inset of Fig. 15(a). It is noted that these peak positions are nearly unchanged whatever temperature is changed. On the other hand, the bend in M_{a^*} is confirmed to be a discontinuous change of dM_{a^*}/dH, although it is dull. Its position shifts to the lower field side with increasing temperature and then vanishes. Here, first, we will examine the cause of the magnetization step using Fig. 10. Considering the three structural domains, the fact that the magnetic field is applied along the a^* axis is equivalent to the fact that it is applied in each of the 30°, 90°, and 150° directions in Fig. 10 as said before. At 90°, it can be easily imagined from Figs. 10 and 8(a) that the phase transition occurs in a magnetic field of about $0.9 \sim 1$ T, and it can be concluded that the magnetization step at about 0.9 T is the first-order phase transition from phase I to phase II. On the other hand, the situation is a little complicated for 30° and 150°. If the direction of the magnetic field is deviated by a slight positive angle $\Delta\theta$ from a^* axis, the phase transition does not occur in the domain corresponding to $150° + \Delta\theta$.

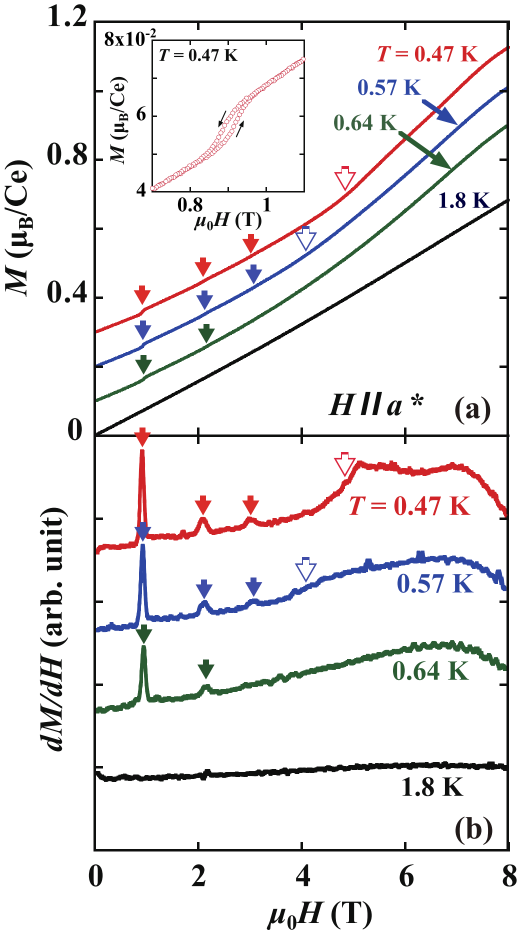

FIG. 15. (a) The magnetization isotherms of $CeZn_3P_3$ at several temperatures below 1.8 K in magnetic fields along the a^* axis. Each magnetization curve is shifted along the vertical axis by multiplicative factors of $0.1\,\mu_B$. Arrows below and above $\mu_0 H = 4$ T indicate the position of steps and kinks of the magnetization curve, respectively. Inset displays magnified magnetization isotherm around $\mu_0 H = 0.9$ T which distinctly shows the hysteresis suggesting the first-order phase transition. (b) Field derivative of the magnetization of $CeZn_3P_3$ (dM/dH). Peaks of dM/dH shown by arrows below 4 T correspond to the magnetization step in the upper panel, while the steps of dM/dH shown by arrows above 4 T suggest the second-order phase transition, although they are rather gradual.

However, in the domain corresponding to $30^\circ + \Delta\theta$, it is expected that the phase transition will occur in a magnetic field much larger than 0.9 T as expected from Fig. 10. Therefore, these additional steps in Fig. 15(a) and additional peaks in Fig. 15(b) around 2.1 T and 3 T are considered to be caused by this angular deviation. In other words, it might be because multiple crystals are used together. On the other hand, the bending of the magnetization is considered to be a phase transition from phase II to phase III, judging from the magnitude of the magnetic field. This phase transition is characterized by a larger magnetization slope in phase III. Further application of the magnetic field should cause a transition to the paramagnetic phase, but unfortunately, the performance of the superconducting magnet used did not allow sufficient application of the magnetic field in the experiment. Anyway, these results mentioned so far remind us of $YbAl_3C_3$ with the same $ScAl_3C_3$ structure again. Assuming that the dimer phase of $YbAl_3C_3$ corresponds to the antiferromagnetic phase of $CeZn_3P_3$ (phase I and II), phase III and/or III′ is considered to correspond to the field-induced disordered phase (FIDP) of $YbAl_3C_3$, and then both compounds undergo the transition to the field-induced ferromagnetic phase with increasing magnetic field. Here, we should note that the increase of the magnetization in phase III and/or III′ is more pronounced than those in the other phases, suggesting that ferromagnetic components are mixed in this phase, which is also similar to $YbAl_3C_3$. In the case of magnetic field along the a axis, which is not shown, only one step was observed as expected from Fig. 10.

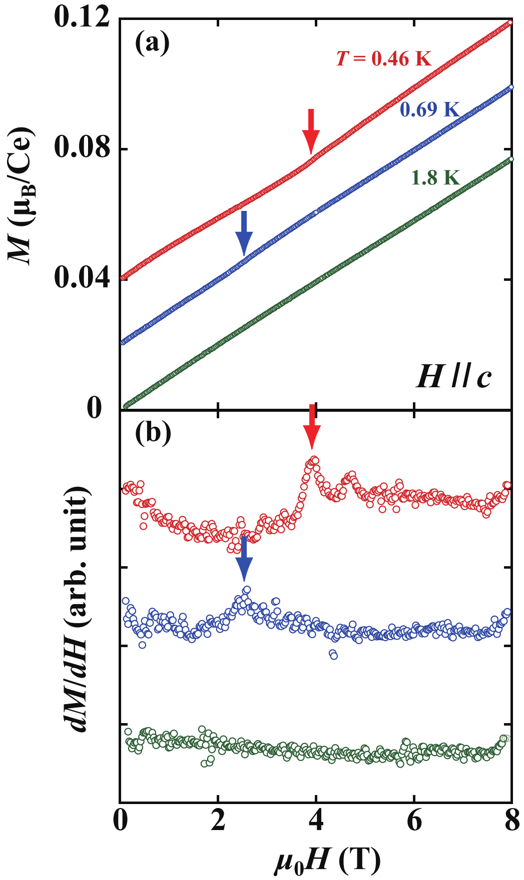

FIG. 16. (a) The magnetization isotherms of $CeZn_3P_3$ at several temperatures below 1.8 K in magnetic fields along the c axis. Each magnetization curve is shifted along the vertical axis by multiplicative factors of $0.02\,\mu_B$. Arrows indicate a kink of the magnetization curve. (b) Field derivative of the magnetization of $CeZn_3P_3$ (dM/dH). Peaks of dM/dH shown by arrows correspond to the kink of the magnetization curve in the upper panel.

In contrast to M_{a^*}, the magnetization measured in magnetic fields along the c axis (M_c) is very small reflecting the easy-plane-type magnetic anisotropy of this compound as shown in Fig. 16(a). M_c seems to increase monotonically with increasing magnetic field. Checking it in detail, a tiny change of M_c seems to be recognized as shown by arrows. Figure 16(b) shows the field derivative of the magnetization of $CeZn_3P_3$ measured in $H \parallel c$ (dM_c/dH). Corresponding to the tiny change of M_c, a peak of dM_c/dH seems to be recognized.

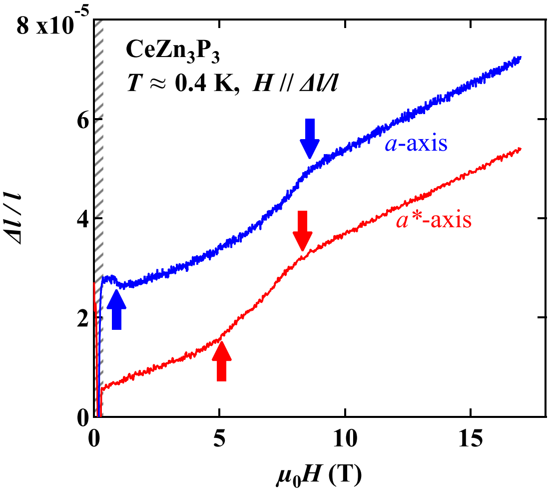

FIG. 17. Field dependence of $\Delta l/l$ along the *a*-axis direction under $H \parallel a$ and a^*-axis direction under $H \parallel a^*$ at $T \approx 0.4$ K. The gray shaded area indicates low accuracy region due to the influence of the large magnetic resistance of the strain gauge.

However, considering the magnitude of M_c, which is one order of magnitude smaller than M_{a^*}, the change may be within the error range, so we will give no further consideration at the present stage.

2. *Magnetostriction of* CeZn$_3$P$_3$ *at low temperatures*

The magnetostriction measurement was performed using a strain gauge at low temperatures. Figure 17 shows the magnetic-field dependence of the relative expansion (magnetostriction, $\Delta l/l$) using one piece of crystal. The direction of $\Delta l/l$ is the same with that of the applied field. Here, we note that the crystal is formed from three domains. Therefore, it is difficult to draw a completely assertive conclusion, but there are some obvious things. In fact, when making the phase diagram of this system, we learned that this material is strongly influenced by the multiple domains reflecting the symmetry of the orthorhombic structure in the low magnetic field region, resulting in superposition of multiple phenomena in different directions, however, in the high magnetic field region, it seems that it reflects the symmetry of the original hexagonal crystal and makes the influence of the multiple domains almost insensitive. First, when examining the low magnetic field region, a jump near discontinuity around $\mu_0 H \sim 1$ T is observed in the expansion coefficient in the *a*-axis direction. On the other hand, almost no anomaly around $\mu_0 H \sim 1$ T can be seen in the expansion coefficient in the *a**-axis direction. Considering the experimental results so far, it seems that this discontinuous jump in the expansion coefficient in the *a*-axis direction corresponds to the first-order phase transition from phase I to the phase II. In the case of the *a**-axis direction, if the boundary between phase I and phase II is traced when the magnetic field increases, no major anomaly may be visible. In any case, the superposition of the three domains may obscure the anomaly. On the other hand, the anomaly of the magnetostriction corresponding to the transition or crossover becomes clear in the high magnetic field region. When the magnetic field is applied along the *a**-axis direction, clear bends are visible in the magnetostriction as shown by the arrows in the figure, corresponding to crossing the two boundaries of about 5 T and about 8 T in Fig. 10. When the magnetic field is applied along the *a*-axis direction, $\Delta l/l$ gradually rises and bends at about 8.5 T, which is a boundary with the paramagnetic region.

E. Ground state of CeZn$_3$P$_3$ at low temperatures

From the experimental results so far, it is clear that the rotational symmetry around the *c* axis of CeZn$_3$P$_3$ may drop from sixfold symmetry (exactly saying threefold spiral symmetry) to a twofold one. In addition, the activation-type electrical resistivity means that the magnetic interaction between Ce layers, of which interval is as much as 10 Å, is very weak because relatively long-range RKKY interaction does not work due to the lack of carriers. Therefore, to discuss the magnetic properties of Ce ions, it would be better to treat them as forming a slightly distorted two-dimensional triangular lattice. So, the sides of the triangle, i.e., bonds between Ce ions are no longer equivalent. As a result, the magnitude of the magnetic interaction is also unequal, corresponding to the three different bonds. If such a bond is not connected to a bond of the same type, dimer formation may be possible, similar to YbAl$_3$C$_3$. In fact, considering several similarities with YbAl$_3$C$_3$ mentioned above, it seems meaningful to examine the physical properties of CeZn$_3$P$_3$ based on the magnetic dimer state.

First, we show the result of the low-temperature specific heat calculated by the isolated dimer model by the green solid line in Fig. 3. Here, the splitting energy between the singlet and triplet is set to 3.4 K, which is the same as the value using in the magnetic susceptibility calculation described later. As understood by the figure, since the experimental results are more spread than the calculated results, assuming the dimer formation, energy dispersion due to the interaction between dimers is recalled. So, we will try to explain its magnetic susceptibilities at low temperatures by an interacting dimer model. The magnetic susceptibility of the isolated dimer model can be written as follows:

$$\chi_d \sim \frac{M_d}{H} = \frac{N_\mathrm{A}}{2}\frac{g\mu_\mathrm{B}}{H}\frac{\sum_{s^z=-1}^{1}[s^z e^{-\beta(\Delta+g\mu_\mathrm{B}s^z H)}]}{Z}, \tag{12}$$

where N_A is the Avogadro constant, g and μ_B are g factor and Bohr-magneton, respectively, and Δ is the intradimer exchange coupling parameter, i.e., singlet-triplet splitting. The partition function Z is written as

$$Z = 1 + \sum_{s^z=-1}^{1} e^{-\beta(\Delta+g\mu_\mathrm{B}s^z H)}. \tag{13}$$

For fitting of the actual magnetic susceptibility, the contribution from the interdimer interaction (γ), the van-Vleck-type susceptibility (χ_0), and the magnetic impurities (C_i/T) are introduced as additional parameters, and the following expression is used:

$$\chi = \frac{\chi_\mathrm{d}}{1-\gamma\chi_\mathrm{d}} + \chi_0 + C_i/T. \tag{14}$$

Fitting results are shown by dotted lines in Fig. 4 and fitting parameters are summarized in Table II. Calculated susceptibilities well reproduce the experimental results at low

TABLE II. Parameters used for the fitting of $M(T)/H$ measured in $\mu_0 H = 1$ T in low temperatures assuming an interacting dimer model composed of the $S = \frac{1}{2}$ spin pair.

	Δ (K)	g factor	γ (mol/emu)	χ_0 (emu/mol)	C_i (emu K/mol)
$\chi_{\parallel a^*}$	3.4	1.9	−13	0.003	0.003
$\chi_{\parallel c}$	3.4	0.4	−210	0.002	0.003

temperatures. Here are some points to be noted about the fitting parameters.

(1) The susceptibilities of both directions are well reproduced by using the same parameter Δ of the singlet-triplet splitting. Anisotropic interactions such as Ising or XY types interaction should cause different splitting from that of Heisenberg type. Therefore, this result suggests the exchange Hamiltonian is rather isotropic, i.e., Heisenberg-type exchange interaction.

(2) The g factor, which is also a fitting parameter, is obtained with almost the same anisotropy as the g factor of the ground-state doublet obtained by the crystal-field analysis, $g_{\parallel c} = 0.393$ and $g_{\perp c} = 1.95$, as described before.

(3) The molecular field constant γ is not only proportional to the exchange coupling constant but also includes g^{-2} [27,28]. Taking the contribution from the anisotropic g factor into account, it can be seen that the exchange interaction expected from the obtained anisotropic γ parameter is almost isotropic. Since the exchange interaction that contributes to γ is that between dimers, this suggests that not only the intradimer exchange interaction but also the interdimer exchange interaction is Heisenberg type. Also, the non-negligible interdimer exchange interaction may be the cause of the appearance of the magnetic order in $\mathrm{CeZn_3P_3}$, unlike $\mathrm{YbAl_3C_3}$.

(4) The contribution from magnetic impurities (C_i/T) plays an important role. The estimated C_i value is much smaller than that in the case of $\mathrm{YbAl_3C_3}$, and assuming isolated $\mathrm{Ce^{3+}}$ free ions as its origin, it is estimated that only about 0.4% of the $\mathrm{Ce^{3+}}$ ion contributes. Nevertheless, it may have a significant effect on the magnetic susceptibility along the c axis (M_c/H) due to the small magnitude of M_c/H. In the case of M/H along the a^* axis (M_{a^*}/H) in the low-temperature paramagnetic region shown in Fig. 14(a), it can be seen that the magnitude of M_{a^*}/H increases with the magnetic field. Assuming a dimer model, this can be understood as the process in which the singlet ground state is destroyed by applying magnetic field because intrinsic susceptibility may be dominant along the a^* axis due to the large g factor. In contrast, the Curie-type susceptibility due to magnetic impurities is dominant in the c axis, and therefore M_c/H increases with decreasing temperature. However, as the magnetic field increases, the contribution from the magnetic impurities levels off, so the magnetic susceptibility decreases. At this time, since the g factor along the c axis is small, its original dimer energy scheme, i.e., the singlet-triplet splitting, remains up to a high magnetic field. This is probably the reason why a broad peak structure is observed even in a high magnetic field.

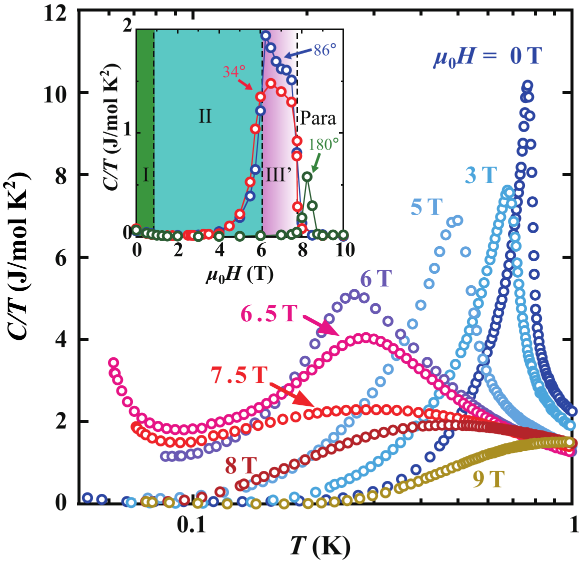

FIG. 18. Temperature dependence of C/T in several selected magnetic fields along the c plane with $\theta = 86^\circ$ with regarding to the majority domain. The inset shows the magnetic field dependence of C/T at 0.1 K in magnetic field angle of $\theta = 34^\circ$, 86°, and 180°. The areas displayed in the inset correspond to the phases when the direction of the magnetic field is 86° or 34°; see Fig. 13 for those of the 180° direction.

In $\mathrm{YbAl_3C_3}$, when the dimer state was broken by the magnetic field, a strange phase, FIDP [15], which exhibits a similar physical property such as an anomalous increase, proportional to $-\ln T$ of C/T to those of the non-Fermi liquid state of the heavy Fermion system appeared. Furthermore, its strange phase is characterized by appearing in a wide magnetic field range rather than around the singularity point of the magnetic field. Assuming that the dimer state of $\mathrm{YbAl_3C_3}$ corresponds to the magnetically ordered phase (phase I and II) of $\mathrm{CeZn_3P_3}$, FIDP of $\mathrm{YbAl_3C_3}$ seems to correspond to phase III and/or III′, as said before. Phase III and/or III′ is similar to FIDP of $\mathrm{YbAl_3C_3}$ in that it not only appears in a wide magnetic field range but is not closed in the $H - T$ phase diagram. Therefore, we reexamine the specific heat of $\mathrm{CeZn_3P_3}$ at low temperatures. Figure 18 shows the temperature dependence of the specific heat divided by the temperature (C/T) in several selected magnetic fields with a field angle $\theta = 86^\circ$ on the c plane. The magnetic field dependence of C/T at $T = 0.1$ K is shown in the inset, accompanied with those with field angles $\theta = 34^\circ$ and 180°. In the magnetic field region corresponding to phase I or II, C/T becomes almost zero at low temperatures after forming a clear peak corresponding to the magnetic phase transition. With increasing magnetic field and approaching the boundary with the phase III′, C/T at low temperatures begins to increase, and in phase III′, it becomes as large as $1 \sim 2$ J mol^{-1}K^{-2} at $T = 0.1$ K as shown in the inset. In addition, upturns of C/T are observed at lower temperatures in phase III′. When the magnetic field is further applied and exceeds about 8 T, the paramagnetic phase appears where the Schottky-type specific heat characterized by the Zeeman splitting is observed and C/T becomes almost zero at low temperatures similar to phase I or II. Usually, the upturn of the specific heat at low temperatures is often regarded as a contribution from the nuclear specific heat. However, since the upturn tends to disappear in the paramagnetic region of higher magnetic fields, this seems to be a phenomenon peculiar to this region of phase III′ due to some disorder. Similar behavior is also observed when the magnetic field is applied along the angle of $\theta = 34^\circ$ on the c plane. However, when the field is applied along $\theta = 180^\circ$, i.e., along the a axis, an abnormal increase of C/T is hardly observed except several traces near $\mu_0 H = 8.5$ T. The abnormal increase of C/T with decreasing temperature is also a common phenomenon with $YbAl_3C_3$.

FIDP of $YbAl_3C_3$ has been interestingly pointed out by neutron-scattering experimental studies [29]. The analysis of the neutron diffraction pattern under magnetic field suggested admixture of possible two magnetic configurations in FDIP, which signifies the resurrection of their degeneracy. In other words, it points to the fact that the geometrical frustration is recovered by applying magnetic field. It's unclear whether a similar state is established in $CeZn_3P_3$, but an interesting phenomenon related to this could be pointed out. It is the restoration of symmetry before deformation by applying a magnetic field. As shown in Fig. 10, phase III or III′ is surrounded by the borders represented by Eqs. (8) and (9) with sixfold symmetry. Therefore, phase III or III′ has the same geometric frustration due to sixfold symmetry as before the deformation, so some degree of degeneracy may exist even at low temperatures.

Finally, let us discuss the difference in magnetism between the d-electron system and the f-electron system, which are related to this study. As seen in the Appendix, considering the Kramers doublet ground state of the one $4f$-electron system of the Ce^{3+} ion, when the Ce^{3+} ions on both ends of the line segment and the interaction Hamiltonian between the Ce^{3+} ions have the same rotational symmetry around the segment, the exchange interaction between the Ce^{3+} ions is substantially the same as that of the isotropic $S = 1/2$ spin system under the assumption that the influence of the excited state can be ignored and the inversion symmetry exists at the middle of the segment. In fact, as shown in Table I, the first excited state seems to be located more than 300 K far from the doublet ground state, and there is an inversion center at themiddle of the line segment under the hexagonal crystal symmetry. Therefore, the only difference from the d-electron $S = 1/2$ spin system is the anisotropy of the g factor in Zeeman energy. In the case of the objective compound this time, ignoring small deformations, the g factor should be isotropic in the c plane while the magnetic field is small. It means the appearance of concentric phase boundaries. In reality, as shown in Fig. 10 of the magnetic field strength-direction phase diagram, the boundary between regions I and II is twofold symmetric reflecting the deformation in the low magnetic field region, but the boundaries on both sides of phase III recover the sixfold symmetry. In any case, it is interpreted that the symmetry of the system strongly appears in the symmetry of the boundary, which means that the orbital wave function plays a major role in the restoration of symmetry. In addition, it means that the orbit is largely involved in the residual degeneracy.

IV. CONCLUSION

Magnetic properties of $CeZn_3P_3$ have been investigated by magnetization (M), magnetostriction, specific heat (C), and magnetocaloric effect measurements. In the process of this investigation, we have found that $CeZn_3P_3$, which has been believed to have the same hexagonal $ScAl_3C_3$-type crystal structure as $YbAl_3C_3$, certainly has a slightly deformed crystal structure, possibly orthorhombic one, even at room temperature by the magnetic field direction dependence of the C. This is in contrast to $YbAl_3C_3$ and the isomorphic Ce compounds of $CeCd_3P_3$ and $CeCd_3As_3$ undergoing a structural phase transition at 80 K and around 130 K, respectively. Furthermore, we found that $CeZn_3P_3$ forms a structural domain similar to that of the low-temperature phase of $YbAl_3C_3$. In contrast to the nonmagnetic ground state of $YbAl_3C_3$ due to the dimer formation, $CeZn_3P_3$ shows a magnetic order below $T_N = 0.8$ K. The analysis of the temperature dependence of the magnetic susceptibility (χ) and C has revealed that a Kramers doublet ground state with an easy-plane-type magnetic anisotropy on the c plane is well isolated from the excited states by the crystal field splitting energy of more than 300 K. Above $T_N = 0.8$ K, $\chi_{\parallel a^*}$ makes a broad peak at around 2 K, which is related to the shoulder structure of C at several Kelvin and is certainly originated from the dimer formation due to the slight deformation of the triangular lattice being similar to $YbAl_3C_3$. On the other hand, the reason why the shoulder structure cannot be seen in $\chi_{\parallel c}$ is considered to be concealed by the magnetism of impurities, and it is presumed that the Hamiltonian of this system is Heisenberg type despite the anisotropic magnetic moment. Below T_N, a magnetic phase diagram reminiscent of a magnetic flower blooming on the c plane was observed, which may have a close relation to a quantum effect of a quasi $S = \frac{1}{2}$ spin system and a contribution of the orbital component. With increasing magnetic field, we have found an anomalous magnetic state beyond the usual magnetically ordered state, where anomalously enhanced C/T is observed. This anomalous magnetic state is similar to FIDP observed in $YbAl_3C_3$ induced by magnetic field, although the magnetic ground state in $YbAl_3C_3$ is a nonmagnetic dimer state different from the normal magnetically ordered state in $CeZn_3P_3$.

ACKNOWLEDGMENTS

One of the authors would like to thank K. Hara for his pioneering research on the compound $CeZn_3P_3$. The authors would like to thank N. Fukiage, M. Moriyama, and M. Kikuchi for their technical support.

APPENDIX

We consider the exchange interaction in $CeZn_3P_3$. The following discussion is in accordance with Ref. [7]. Assuming $|n, \pm\rangle$ as a ground-state Kramers doublet, where n indicates the position of Ce^{3+} ion, we derive an effective Hamiltonian $\mathcal{H}_{\mathrm{eff}}$ to describe the exchange interactions between neighboring Ce^{3+} ions at position 1 [Ce(1)] and position 2 [Ce(2)] on the a axis using second-order perturbation. Here, we ignore the slight deformation of the crystal structure and restrict the energy region below CEF splitting.

Let $\mathcal{H}_{2,1}$ be the hopping Hamiltonian between Ce(1) and Ce(2). First, we define the creation and annihilation operator of an electron in $\pm$ state of Ce(n) as $f^\dagger_{n\pm}$ and $f_{n\pm}$, respectively. The $+$ and $-$ states correspond to the up state and down state of the effective spin of the Kramers doublet introduced later. Considering all hopping processes, we obtain an effective interaction Hamiltonian $\mathcal{H}_{\mathrm{eff}} \propto \mathcal{H}^1_{\mathrm{eff}} + \mathcal{H}^2_{\mathrm{eff}} + \mathcal{H}^3_{\mathrm{eff}}$ as follows:

$$\begin{aligned}
\mathcal{H}^1_{\mathrm{eff}} = &-\langle 1,+|\mathcal{H}_{2,1}|2,+\rangle\langle 2,+|\mathcal{H}_{2,1}|1,+\rangle f^{\dagger}_{1+}f_{2+}f^{\dagger}_{2+}f_{1+}\\
&-\langle 2,+|\mathcal{H}_{2,1}|1,+\rangle\langle 1,+|\mathcal{H}_{2,1}|2,+\rangle f^{\dagger}_{2+}f_{1+}f^{\dagger}_{1+}f_{2+}\\
&-\langle 1,+|\mathcal{H}_{2,1}|2,+\rangle\langle 2,-|\mathcal{H}_{2,1}|1,-\rangle f^{\dagger}_{1+}f_{2+}f^{\dagger}_{2-}f_{1-}\\
&-\langle 1,-|\mathcal{H}_{2,1}|2,-\rangle\langle 2,+|\mathcal{H}_{2,1}|1,+\rangle f^{\dagger}_{1-}f_{2-}f^{\dagger}_{2+}f_{1+}\\
&-\langle 2,+|\mathcal{H}_{2,1}|1,+\rangle\langle 1,-|\mathcal{H}_{2,1}|2,-\rangle f^{\dagger}_{2+}f_{1+}f^{\dagger}_{1-}f_{2-}\\
&-\langle 2,-|\mathcal{H}_{2,1}|1,-\rangle\langle 1,+|\mathcal{H}_{2,1}|2,+\rangle f^{\dagger}_{2-}f_{1-}f^{\dagger}_{1+}f_{2+}\\
&-\langle 1,-|\mathcal{H}_{2,1}|2,-\rangle\langle 2,-|\mathcal{H}_{2,1}|1,-\rangle f^{\dagger}_{1-}f_{2-}f^{\dagger}_{2-}f_{1-}\\
&-\langle 2,-|\mathcal{H}_{2,1}|1,-\rangle\langle 1,-|\mathcal{H}_{2,1}|2,-\rangle f^{\dagger}_{2-}f_{1-}f^{\dagger}_{1-}f_{2-}.
\end{aligned} \tag{A1}$$

$$\begin{aligned}
\mathcal{H}^2_{\mathrm{eff}} = &-\langle 1,+|\mathcal{H}_{2,1}|2,+\rangle\langle 2,+|\mathcal{H}_{2,1}|1,-\rangle f^{\dagger}_{1+}f_{2+}f^{\dagger}_{2+}f_{1-}\\
&-\langle 2,+|\mathcal{H}_{2,1}|1,-\rangle\langle 1,+|\mathcal{H}_{2,1}|2,+\rangle f^{\dagger}_{2+}f_{1-}f^{\dagger}_{1+}f_{2+}\\
&-\langle 1,-|\mathcal{H}_{2,1}|2,-\rangle\langle 2,+|\mathcal{H}_{2,1}|1,-\rangle f^{\dagger}_{1-}f_{2-}f^{\dagger}_{2+}f_{1-}\\
&-\langle 2,+|\mathcal{H}_{2,1}|1,-\rangle\langle 1,-|\mathcal{H}_{2,1}|2,-\rangle f^{\dagger}_{2+}f_{1-}f^{\dagger}_{1-}f_{2-}\\
&-\langle 2,+|\mathcal{H}_{2,1}|1,+\rangle\langle 1,-|\mathcal{H}_{2,1}|2,+\rangle f^{\dagger}_{2+}f_{1+}f^{\dagger}_{1-}f_{2+}\\
&-\langle 1,-|\mathcal{H}_{2,1}|2,+\rangle\langle 2,+|\mathcal{H}_{2,1}|1,+\rangle f^{\dagger}_{1-}f_{2+}f^{\dagger}_{2+}f_{1+}\\
&-\langle 2,-|\mathcal{H}_{2,1}|1,-\rangle\langle 1,-|\mathcal{H}_{2,1}|2,+\rangle f^{\dagger}_{2-}f_{1-}f^{\dagger}_{1-}f_{2+}\\
&-\langle 1,-|\mathcal{H}_{2,1}|2,+\rangle\langle 2,-|\mathcal{H}_{2,1}|1,-\rangle f^{\dagger}_{1-}f_{2+}f^{\dagger}_{2-}f_{1-}\\
&-\langle 1,+|\mathcal{H}_{2,1}|2,+\rangle\langle 2,-|\mathcal{H}_{2,1}|1,+\rangle f^{\dagger}_{1+}f_{2+}f^{\dagger}_{2-}f_{1+}\\
&-\langle 2,-|\mathcal{H}_{2,1}|1,+\rangle\langle 1,+|\mathcal{H}_{2,1}|2,+\rangle f^{\dagger}_{2-}f_{1+}f^{\dagger}_{1+}f_{2+}\\
&-\langle 1,-|\mathcal{H}_{2,1}|2,-\rangle\langle 2,-|\mathcal{H}_{2,1}|1,+\rangle f^{\dagger}_{1-}f_{2-}f^{\dagger}_{2-}f_{1+}\\
&-\langle 2,-|\mathcal{H}_{2,1}|1,+\rangle\langle 1,-|\mathcal{H}_{2,1}|2,-\rangle f^{\dagger}_{2-}f_{1+}f^{\dagger}_{1-}f_{2-}\\
&-\langle 2,+|\mathcal{H}_{2,1}|1,+\rangle\langle 1,+|\mathcal{H}_{2,1}|2,-\rangle f^{\dagger}_{2+}f_{1+}f^{\dagger}_{1+}f_{2-}\\
&-\langle 1,+|\mathcal{H}_{2,1}|2,-\rangle\langle 2,+|\mathcal{H}_{2,1}|1,+\rangle f^{\dagger}_{1+}f_{2-}f^{\dagger}_{2+}f_{1+}\\
&-\langle 2,-|\mathcal{H}_{2,1}|1,-\rangle\langle 1,+|\mathcal{H}_{2,1}|2,-\rangle f^{\dagger}_{2-}f_{1-}f^{\dagger}_{1+}f_{2-}\\
&-\langle 1,+|\mathcal{H}_{2,1}|2,-\rangle\langle 2,-|\mathcal{H}_{2,1}|1,-\rangle f^{\dagger}_{1+}f_{2-}f^{\dagger}_{2-}f_{1-}.
\end{aligned} \tag{A2}$$

$$\begin{aligned}
\mathcal{H}^3_{\mathrm{eff}} = &-\langle 1,-|\mathcal{H}_{2,1}|2,+\rangle\langle 2,+|\mathcal{H}_{2,1}|1,-\rangle f^{\dagger}_{1-}f_{2+}f^{\dagger}_{2+}f_{1-}\\
&-\langle 1,+|\mathcal{H}_{2,1}|2,-\rangle\langle 2,+|\mathcal{H}_{2,1}|1,-\rangle f^{\dagger}_{1+}f_{2-}f^{\dagger}_{2+}f_{1-}\\
&-\langle 2,+|\mathcal{H}_{2,1}|1,-\rangle\langle 1,-|\mathcal{H}_{2,1}|2,+\rangle f^{\dagger}_{2+}f_{1-}f^{\dagger}_{1-}f_{2+}\\
&-\langle 2,-|\mathcal{H}_{2,1}|1,+\rangle\langle 1,-|\mathcal{H}_{2,1}|2,+\rangle f^{\dagger}_{2-}f_{1+}f^{\dagger}_{1-}f_{2+}\\
&-\langle 1,+|\mathcal{H}_{2,1}|2,-\rangle\langle 2,-|\mathcal{H}_{2,1}|1,+\rangle f^{\dagger}_{1+}f_{2-}f^{\dagger}_{2-}f_{1+}\\
&-\langle 1,-|\mathcal{H}_{2,1}|2,+\rangle\langle 2,-|\mathcal{H}_{2,1}|1,+\rangle f^{\dagger}_{1-}f_{2+}f^{\dagger}_{2-}f_{1+}\\
&-\langle 2,-|\mathcal{H}_{2,1}|1,+\rangle\langle 1,+|\mathcal{H}_{2,1}|2,-\rangle f^{\dagger}_{2-}f_{1+}f^{\dagger}_{1+}f_{2-}\\
&-\langle 2,+|\mathcal{H}_{2,1}|1,-\rangle\langle 1,+|\mathcal{H}_{2,1}|2,-\rangle f^{\dagger}_{2+}f_{1-}f^{\dagger}_{1+}f_{2-}.
\end{aligned} \tag{A3}$$

Here we replace the products of $f^{\dagger}_{n\pm}$ and $f_{n\pm}$ with effective spin s_n as follows:

$$f^{\dagger}_{n\pm}f_{n\pm} \rightarrow \pm s^z_n + \tfrac{1}{2}, \quad f^{\dagger}_{n+}f_{n-} \rightarrow s^+_n, \quad f^{\dagger}_{n-}f_{n+} \rightarrow s^-_n. \tag{A4}$$

Then, we obtain the following representations for $\mathcal{H}^1_{\mathrm{eff}}$, $\mathcal{H}^2_{\mathrm{eff}}$, and $\mathcal{H}^3_{\mathrm{eff}}$:

$$\begin{aligned}
\mathcal{H}^1_{\mathrm{eff}} = {}& 2(|\langle 2,+|\mathcal{H}_{2,1}|1,+\rangle|^2 + |\langle 2,-|\mathcal{H}_{2,1}|1,-\rangle|^2)\big(s^z_1 s^z_2 - \tfrac{1}{4}\big)\\
&+ 4\mathrm{Re}(\langle 2,-|\mathcal{H}_{2,1}|1,-\rangle\langle 1,+|\mathcal{H}_{2,1}|2,+\rangle)\big(s^x_1 s^x_2 + s^y_1 s^y_2\big)\\
&+ 4\mathrm{Im}(\langle 2,-|\mathcal{H}_{2,1}|1,-\rangle\langle 1,+|\mathcal{H}_{2,1}|2,+\rangle)(\mathbf{s}_1 \times \mathbf{s}_2)_z,
\end{aligned} \tag{A5}$$

where Re and Im are real and imaginary parts, respectively, and the last term corresponds to the Dzyaloshinsky-Moriya (DM) interaction with a characteristic **D** vector pointing in the z direction:

$$\begin{aligned}
\mathcal{H}^2_{\mathrm{eff}} = &-[2(\langle 1,-|\mathcal{H}_{2,1}|2,-\rangle^{*}\langle 2,-|\mathcal{H}_{2,1}|1,+\rangle^{*}\\
&- \langle 1,+|\mathcal{H}_{2,1}|2,+\rangle\langle 2,+|\mathcal{H}_{2,1}|1,-\rangle)s^+_1 s^z_2\\
&+ 2(\langle 1,-|\mathcal{H}_{2,1}|2,-\rangle\langle 2,-|\mathcal{H}_{2,1}|1,+\rangle\\
&- \langle 1,+|\mathcal{H}_{2,1}|2,+\rangle^{*}\langle 2,+|\mathcal{H}_{2,1}|1,-\rangle^{*})s^-_1 s^z_2\\
&+ 2(\langle 1,-|\mathcal{H}_{2,1}|2,-\rangle\langle 2,+|\mathcal{H}_{2,1}|1,-\rangle\\
&- \langle 1,+|\mathcal{H}_{2,1}|2,+\rangle^{*}\langle 2,-|\mathcal{H}_{2,1}|1,+\rangle^{*})s^+_2 s^z_1\\
&+ 2(\langle 1,-|\mathcal{H}_{2,1}|2,-\rangle^{*}\langle 2,+|\mathcal{H}_{2,1}|1,-\rangle^{*}\\
&- \langle 1,+|\mathcal{H}_{2,1}|2,+\rangle\langle 2,-|\mathcal{H}_{2,1}|1,+\rangle)s^-_2 s^z_1],
\end{aligned} \tag{A6}$$

$$\begin{aligned}
\mathcal{H}^3_{\mathrm{eff}} = &-|\langle 2,+|\mathcal{H}_{2,1}|1,-\rangle|^2\big(\tfrac{1}{2} + 2s^z_1 s^z_2\big)\\
&- 2\langle 1,+|\mathcal{H}_{2,1}|2,-\rangle\langle 2,+|\mathcal{H}_{2,1}|1,-\rangle s^+_1 s^+_2\\
&- |\langle 2,-|\mathcal{H}_{2,1}|1,+\rangle|^2\big(\tfrac{1}{2} + 2s^z_1 s^z_2\big)\\
&- 2\langle 2,-|\mathcal{H}_{2,1}|1,+\rangle\langle 1,-|\mathcal{H}_{2,1}|2,+\rangle s^-_1 s^-_2.
\end{aligned} \tag{A7}$$

Then we consider a concrete exchange interaction along the a axis in $\mathrm{CeZn_3P_3}$. As the midpoint of the segment connecting Ce(1) and Ce(2) ions along the a axis is an inversion center; the Hamiltonian $\mathcal{H}_{2,1}$ should have the inversion symmetry. Then, the following are obtained:

$$\begin{aligned}
\langle 2,\pm|\mathcal{H}_{2,1}|1,\pm\rangle &= \langle 1,\pm|\mathcal{H}_{2,1}|2,\pm\rangle\\
&= \mathrm{Re}(\langle 2,\pm|\mathcal{H}_{2,1}|1,\pm\rangle),\\
\langle 2,\pm|\mathcal{H}_{2,1}|1,\mp\rangle &= \langle 1,\pm|\mathcal{H}_{2,1}|2,\mp\rangle.
\end{aligned} \tag{A8}$$

By using these, each effective Hamiltonian becomes the following:

$$\begin{aligned}
\mathcal{H}^1_{\mathrm{eff}} = {}& 2(\langle 2,+|\mathcal{H}_{2,1}|1,+\rangle^2 + \langle 2,-|\mathcal{H}_{2,1}|1,-\rangle^2)\big(s^z_1 s^z_2 - \tfrac{1}{4}\big)\\
&+4(\langle 2,-|\mathcal{H}_{2,1}|1,-\rangle\langle 2,+|\mathcal{H}_{2,1}|1,+\rangle)\big(s^x_1 s^x_2 + s^y_1 s^y_2\big).
\end{aligned} \tag{A9}$$

So, the term of the DM interaction vanishes due to the emergence of the inversion symmetry:

$$\begin{aligned}\mathcal{H}_{\text{eff}}^2 = {} & 2\big(\langle 2,+|\mathcal{H}_{2,1}|1,+\rangle - \langle 2,-|\mathcal{H}_{2,1}|1,-\rangle\big)\\ & \times\big[\langle 2,+|\mathcal{H}_{2,1}|1,-\rangle s_1^+ s_2^z + \langle 2,+|\mathcal{H}_{2,1}|1,-\rangle^* s_1^- s_2^z\\ & + \langle 2,+|\mathcal{H}_{2,1}|1,-\rangle s_2^+ s_1^z + \langle 2,+|\mathcal{H}_{2,1}|1,-\rangle^* s_2^- s_1^z\big],\end{aligned} \tag{A10}$$

$$\begin{aligned}\mathcal{H}_{\text{eff}}^3 = {} & -|\langle 2,+|\mathcal{H}_{2,1}|1,-\rangle|^2\big(1+4s_1^z s_2^z\big)\\ & -2\langle 2,+|\mathcal{H}_{2,1}|1,-\rangle^2 s_1^+ s_2^+\\ & -2\langle 2,-|\mathcal{H}_{2,1}|1,+\rangle^2 s_1^- s_2^-.\end{aligned} \tag{A11}$$

To derive a more detailed form of the interaction Hamiltonian along the *a* axis, we examine the form of the wave function. We assume the *a* axis as a quantized *z* axis. Then, the local symmetry of Ce-ion site is regarded as an orthogonal one, which has twofold rotational symmetry around the *a* axis (*z* axis). The CEF Hamiltonian ($H_{\text{cry}}^{\text{ortho}}$) is given as follows:

$$H_{\text{cry}}^{\text{ortho}} = B_2^0 O_2^0 + B_2^2 O_2^2 + B_4^0 O_4^0 + B_4^2 O_4^2 + B_4^4 O_4^4, \tag{A12}$$

where B_l^m represent CEF parameters and O_l^m are Stevens operators. $H_{\text{cry}}^{\text{ortho}}$ splits sixfold degenerated $J = 5/2$ multiplet to three Kramers doublets, of which forms are different from those listed in Eqs. (4)–(6) determined from Eq. (3), but the energy splitting is the same. Considering the $J_+^2 + J_-^2$ term in $H_{\text{cry}}^{\text{ortho}}$, the wave functions of the ground states can be assumed to be

$$|n,\pm\rangle = \alpha\left|\tfrac{5}{2},\pm\tfrac{5}{2}\right\rangle + \beta\left|\tfrac{5}{2},\pm\tfrac{1}{2}\right\rangle + \gamma\left|\tfrac{5}{2},\mp\tfrac{3}{2}\right\rangle. \tag{A13}$$

Using the Clebsch-Gordan coefficients, the wave functions $|n,\pm\rangle$ are represented with orbital angular components and spin angular components as follows:

$$\begin{aligned}|n,+\rangle = {} & -\alpha\frac{1}{\sqrt{7}}|n,2\uparrow\rangle + \alpha\sqrt{\frac{6}{7}}|n,3\downarrow\rangle\\ & -\beta\sqrt{\frac{3}{7}}|n,0\uparrow\rangle + \beta\frac{2}{\sqrt{7}}|n,1\downarrow\rangle\\ & -\gamma\sqrt{\frac{5}{7}}|n,-2\uparrow\rangle + \gamma\sqrt{\frac{2}{7}}|n,-1\downarrow\rangle,\\ |n,-\rangle = {} & -\alpha\sqrt{\frac{6}{7}}|n,-3\uparrow\rangle + \alpha\frac{1}{\sqrt{7}}|n,-2\downarrow\rangle\\ & -\beta\frac{2}{\sqrt{7}}|n,-1\uparrow\rangle + \beta\sqrt{\frac{3}{7}}|n,0\downarrow\rangle\\ & -\gamma\sqrt{\frac{2}{7}}|n,1\uparrow\rangle + \gamma\sqrt{\frac{5}{7}}|n,2\downarrow\rangle,\end{aligned} \tag{A14}$$

where $|n, m\sigma\rangle$ is a wave function of an electron on orbital *m* and spin σ at Ce(*n*). As the *a* axis has twofold rotational symmetry in addition to the inversion center of its midpoint as mentioned before, we require the same symmetry for the hopping Hamiltonian $\mathcal{H}_{2,1}$. Here we assume that $\mathcal{H}_{2,1}$ conserves spin. Then, the following hopping matrix elements are obtained:

$$\begin{aligned}\langle 2,+|\mathcal{H}_{2,1}|1,+\rangle = {} & \langle 2,+|\mathcal{H}_{2,1}|1,+\rangle^* = \langle 2,-|\mathcal{H}_{2,1}|1,-\rangle\\ = {} & \frac{\alpha^2}{7}t_{2,2}^{(2,1)} + \frac{6\alpha^2}{7}t_{3,3}^{(2,1)} + \frac{3\beta^2}{7}t_{0,0}^{(2,1)} + \frac{4\beta^2}{7}t_{1,1}^{(2,1)} + \frac{5\gamma^2}{7}t_{-2,-2}^{(2,1)} + \frac{2\gamma^2}{7}t_{-1,-1}^{(2,1)} + \frac{\alpha\beta\sqrt{3}}{7}\big(t_{2,0}^{(2,1)} + t_{0,2}^{(2,1)}\big)\\ & + \frac{\beta\gamma\sqrt{15}}{7}\big(t_{0,-2}^{(2,1)} + t_{-2,0}^{(2,1)}\big) + \frac{\gamma\alpha\sqrt{5}}{7}\big(t_{-2,2}^{(2,1)} + t_{2,-2}^{(2,1)}\big) + \frac{2\alpha\beta\sqrt{6}}{7}\big(t_{3,1}^{(2,1)} + t_{1,3}^{(2,1)}\big) + \frac{2\beta\gamma\sqrt{2}}{7}\big(t_{1,-1}^{(2,1)} + t_{-1,1}^{(2,1)}\big)\\ & + \frac{2\gamma\alpha\sqrt{3}}{7}\big(t_{-1,3}^{(2,1)} + t_{3,-1}^{(2,1)}\big),\end{aligned} \tag{A15}$$

where $t_{m,m'}^{(2,1)}$ is the hopping integral from orbital m' of Ce(1) to orbital *m* of Ce(2) as described below:

$$t_{m,m'}^{(2,1)} = \int d\mathbf{r}\varphi_m^*(\mathbf{r}-\mathbf{R}_2)\mathcal{H}_{2,1}\varphi_{m'}(\mathbf{r}-\mathbf{R}_1). \tag{A16}$$

Here, $\mathbf{R}_n$ is the position of Ce(*n*) and φ_m is the wave function of the 4*f* *m* orbit. To derive Eq. (A9), we use that $t_{m,m'}^{(2,1)}$ is nonzero under the condition of $m = m'$ (mod 2) considering twofold rotational symmetry of $\mathcal{H}_{2,1}$. Further, using a relation between spherical harmonics, $Y_{lm}^* = (-1)^m Y_{l-m}$, we can get the following relation:

$$\big[t_{m,m'}^{(2,1)}\big]^* = (-1)^{m+m'} t_{-m,-m'}^{(2,1)}. \tag{A17}$$

Using this result, we can derive

$$\langle 2,+|\mathcal{H}_{2,1}|1,-\rangle = \langle 2,-|\mathcal{H}_{2,1}|1,+\rangle = 0. \tag{A18}$$

This result means $\mathcal{H}_{2,1}$ conserves the effective spin.

Using these results, the following expression is obtained as the exchange interaction along the *a* axis. This is a Heisenberg-type exchange interaction Hamiltonian:

$$\mathcal{H}_{\text{eff}} \propto 4\langle 2,+|\mathcal{H}_{2,1}|1,+\rangle^2\big(s_1^x s_2^x + s_1^y s_2^y + s_1^z s_2^z - \tfrac{1}{4}\big). \tag{A19}$$

So, to summarize the above, when the hopping Hamiltonian has the same rotational symmetry around the same axis as that of the magnetic ions concerned and has inversion symmetry, the exchange interaction between the Kramers doublet of the magnetic ions is regarded as a Heisenberg type. Therefore, to introduce asymmetric exchange interaction, higher order interaction should be considered.

[1] Y. Li, G. Chen, W. Tong, L. Pi, J. Liu, Z. Yang, X. Wang, and Q. Zhang, Phys. Rev. Lett. **115**, 167203 (2015).

[2] Y.-D. Li, X. Wang, and G. Chen, Phys. Rev. B **94**, 035107 (2016).

[3] M. Baenitz, P. Schlender, J. Sichelschmidt, Y. A. Onykiienko, Z. Zangeneh, K. M. Ranjith, R. Sarkar, L. Hozoi, H. C. Walker, J.-C. Orain *et al.*, Phys. Rev. B **98**, 220409(R) (2018).

[4] M. Kohgi, K. Iwasa, J.-M. Mignot, A. Ochiai, and T. Suzuki, Phys. Rev. B **56**, R11388 (1997).

[5] A. Ochiai, T. Suzuki, and T. Kasuya, J. Phys. Soc. Jpn. **59**, 4129 (1990).

[6] K. Iwasa, M. Kohgi, A. Gukasov, J.-M. Mignot, N. Shibata, A. Ochiai, H. Aoki, and T. Suzuki, Phys. Rev. B **65**, 052408 (2002).

[7] H. Shiba, K. Ueda, and O. Sakai, J. Phys. Soc. Jpn. **69**, 1493 (2000).

[8] O. Sakai, M. Kohgi, H. Shiba, A. Ochiai, H. Aoki, K. Takegahara, and H. Harima, J. Phys. Soc. Jpn. **69**, 3633 (2000).

[9] A. Ochiai, S. Matsuda, Y. Ikeda, Y. Shimizu, S. Toyoshima, H. Aoki, and K. Katoh, J. Phys. Soc. Jpn. **80**, 123705 (2011).

[10] L. S. Wu, W. J. Gannon, I. A. Zaliznyak, A. M. Tsvelik, M. Brockmann, J.-S. Caux, M. S. Kim, Y. Qiu, J. R. D. Copley, G. Ehlers *et al.*, Science **352**, 1206 (2016).

[11] T. Matsumura, T. Inami, M. Kosaka, Y. Kato, T. Inukai, A. Ochiai, H. Nakao, Y. Murakami, S. Katano, and H. S. Suzuki, J. Phys. Soc. Jpn. **77**, 103601 (2008).

[12] A. Ochiai, T. Inukai, T. Matsumura, A. Oyamada, and K. Katoh, J. Phys. Soc. Jpn. **76**, 123703 (2007).

[13] Y. Kato, M. Kosaka, H. Nowatari, Y. Saiga, A. Yamada, T. Kobiyama, S. Katano, K. Ohoyama, H. S. Suzuki, N. Aso *et al.*, J. Phys. Soc. Jpn. **77**, 053701 (2008).

[14] M. Oshikawa, K. Ueda, H. Aoki, A. Ochiai, and M. Kohgi, J. Phys. Soc. Jpn. **68**, 3181 (1999).

[15] K. Hara, S. Matsuda, E. Matsuoka, K. Tanigaki, A. Ochiai, S. Nakamura, T. Nojima, and K. Katoh, Phys. Rev. B **85**, 144416 (2012).

[16] M. Jaime, V. F. Correa, N. Harrison, C. D. Batista, N. Kawashima, Y. Kazuma, G. A. Jorge, R. Stern, I. Heinmaa, S. A. Zvyagin *et al.*, Phys. Rev. Lett. **93**, 087203 (2004).

[17] A. A. Aczel, Y. Kohama, M. Jaime, K. Ninios, H. B. Chan, L. Balicas, H. A. Dabkowska, and G. M. Luke, Phys. Rev. B **79**, 100409(R) (2009).

[18] S. E. Sebastian, P. A. Sharma, M. Jaime, N. Harrison, V. Correa, L. Balicas, N. Kawashima, C. D. Batista, and I. R. Fisher, Phys. Rev. B **72**, 100404(R) (2005).

[19] A. T. Nientiedt and W. Jeitschko, J. Soild State Chem. **146**, 478 (1999).

[20] N. Kabeya, T. Sakamoto, K. Hara, Y. Hara, S. Nakamura, K. Katoh, and A. Ochiai, J. Phys. Soc. Jpn. **89**, 074707 (2020).

[21] K. W. H. Stevens, Proc. Phys. Soc. A **65**, 209 (1952).

[22] M. T. Hatchings, Solid State Phys. **16**, 227 (1965).

[23] M. Kosaka, Y. Kato, C. Araki, N. Môri, Y. Nakanishi, M. Yoshizawa, K. Ohoyama, C. Martin, and S. W. Tozer, J. Phys. Soc. Jpn. **74**, 2413 (2005).

[24] T. Matsumura, Y. Hayashi, S. Takai, T. Otsubo, S. Matsuda, and A. Ochiai, J. Phys. Soc. Jpn. **84**, 114712 (2015).

[25] J. Lee, A. Rabus, N. R. Lee-Hone, D. M. Broun, and E. Mun, Phys. Rev. B **99**, 245159 (2019).

[26] S. R. Dunsiger, J. Lee, J. E. Sonier, and E. D. Mun, Phys. Rev. B **102**, 064405 (2020).

[27] T. Nakajima, H. Mitamura, and Y. Ueda, J. Phys. Soc. Jpn. **75**, 054706 (2006).

[28] E. C. Samulon, Y.-J. Jo, P. Sengupta, C. D. Batista, M. Jaime, L. Balicas, and I. R. Fisher, Phys. Rev. B **77**, 214441 (2008).

[29] D. D. Khalyavin, D. T. Adroja, P. Manuel, A. Daoud-Aladine, M. Kosaka, K. Kondo, K. A. McEwen, J. H. Pixley, and Q. Si, Phys. Rev. B **87**, 220406(R) (2013).